![CHALMERS UNIVERSITY OF TECHNOLOGY]

High Temperature Corrosion of FeCrAl Alloys in Humidified Environment

The Influence of Silicon and Reactive Elements

Master's Thesis in Materials Chemistry

AINA EDGREN

Department of Chemistry and Chemical Engineering
CHALMERS UNIVERSITY OF TECHNOLOGY
Gothenburg, Sweden 2019

High Temperature Corrosion of FeCrAl Alloys in Humidified Environment
The Influence of Silicon and Reactive Elements
AINA EDGREN

Cover: Fe-oxide covering RE particles at Alloy A197 exposed in air containing 40% H_2O for 200 hours at 600°C.

Abstract

In order to develop new and more robust fuel cell systems it is important to use materials well suited for the application. In this thesis, new alloys for heat exchangers used within such system have been investigated. Since the environment in the heat exchanger is harsh due to elevated temperatur and high steam load in the gas, the material used needs to show excellent corrosion resistance.

In this thesis, two alumina forming FeCrAl alloys with reactive elements, such as Zr or Y, and silicon were investigated. The alloys were exposed at 800 or 600°C in dry air or in air containing 40% H_2O for 20 or 200 hours. The Corrosion products were investigated by SEM, EDX, TEM and XRD. It was shown that the temperature, water vapour and the composition of the alloys affected the results.

Acknowledgement

Contents

Abbreviations

ATR	Auto-Thermal Reforming
BIB	Broad Ion Beam
BSE	Backscattered Electrons
EDX	Energy Dispersive X-ray
FIB	Focused Ion Beam
PHT	Plate Heat Exchanger
RE	Reactive Element
SE	Secondary Electrons
SEM	Scanning Electron Microscopy
TEE	Third Element Effect
STEM	Scanning Transmission Electron Microscopy
XRD	X-ray Diffraction

1

Introduction

1.1 Background

It is widely known that the world is suffering from global warming due to our massive use of fossil fuels. When the fuel either has been burned for heating purposes or used as fuel for vehicles, it ends up as greenhouse gases in the atmosphere. There are many ways to decrease the use of fossil fuel for electricity production, for example by increasing the use of solar and wind-powered plants. For small or mobile applications, like the energy supply in vehicles, the combustion engines used today may be replaced by fuel cells. The energy efficiency of fuel cells is higher compared to combustion engines. However, there are many challenges connected to the development of fuel cell systems. This thesis will focus on a material related question: how does the metal in heat exchangers used in fuel cell systems behave when the system is running? The answer of this question is an important part of the development of new and more robust fuel cell systems.

The environment in such heat exchanger tends to be very harsh. Since the temperature is elevated and the steam load of the gas is high, the material needs to show excellent corrosion resistance. Furthermore, common stainless steels, such as 310S, cannot be used since it is prone to the formation of volatile chromium compounds, poisoning the fuel cell. [1] Instead, iron-based, alumina-forming alloy called FeCrAl, can be used as an alternative. These alloys also contain about 10-20 wt.% chromium in order to support the formation of a protective alumina scale. [2] This scale protects the material from further corrosion and thus making FeCrAl alloys very attractive for heat exchangers. Unfortunately, the material also has some disadvantages. The high aluminium content affects the mechanical properties in a negative way, making it difficult to manufacture components. [2, 3]

1.2 Aim

The aim with this thesis was to investigate the oxidation behaviour of two different FeCrAl alloys. The exposures took place at 600°C and 800°C, in both dry air and air containing 40% water vapour. SEM, EDX, XRD and STEM was used to analyse the oxidation products.

1.3 Heat Exchanger

Heat exchangers are used to transfer heat between two media that could be either gases, liquids or both, separated by a solid material. Heat exchangers are often used in order to increase the efficiency of a system since excess heat can be used to utilise other reactions in the system. Therefore, the needs of an additional heat source can be reduced. [4, 5] Heat exchangers may also be used the other way around: to keeping a material cold by removing the unwanted heat to another medium.

The so called Plate Heat Exchanger (PHE) is a common heat exchanger type. A PHE consists of several plates pressed together by a frame. Every plate has a gasket, creating a thin gap between the plates where the media are allowed to flow. [6] The heat transfer coefficient in the heat exchanger is high due to corrugated plates. Thus, the efficiency of the PHT is high, meaning that the device can be more compact and smaller compared to other heat exchangers. [7] The design of a PHE can be studied in Figure 1.1.
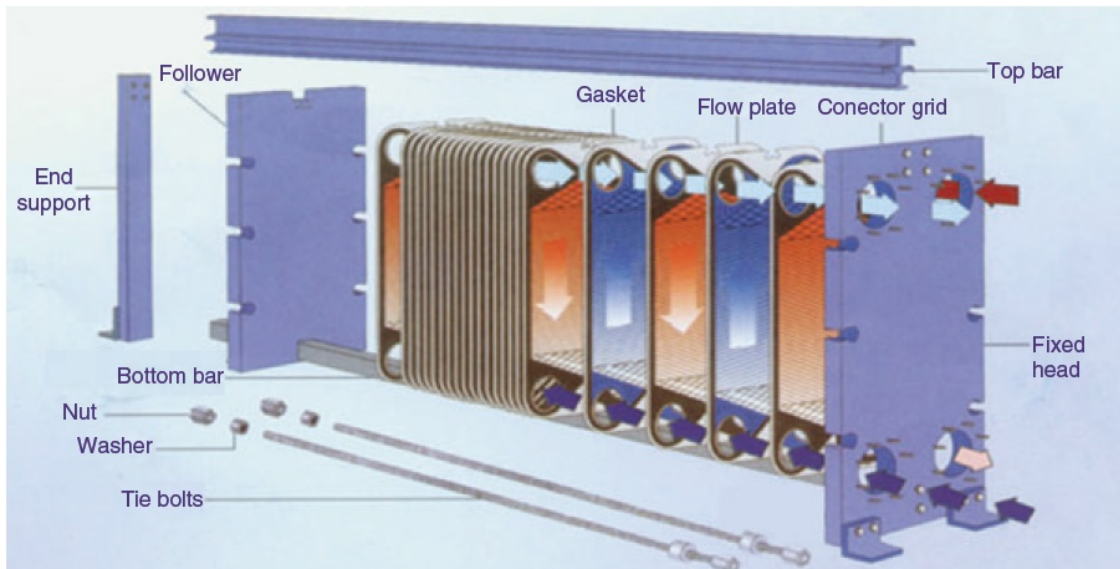
Figure 1.1: Schematic image of a plate heat exchanger.[6]

As mentioned, heat exchangers are used for improving the efficiency of many different sys-

tems. The environment, such as temperature, flow rate and the corrosivity of the media is unique for each application. Therefore, it is important that the material is well suited for the specific application. The aim of this thesis was to investigate alloys for heat exchanger working in a system with fuel cells.

A fuel cell converts chemical energy into electrical energy. The device is fed by a continuous flow of fuel, commonly H_2 due to its very high energy density. [8] The H_2 can be produced in an external H_2 plant and transported to the fuel cell, but since it is complicated to store large quantities of H_2, it is preferred to produce the gas on-demand, in connection to the fuel cell.

One way to do so is to use Auto Thermal Reforming (ATR). In ATR, liquid hydrocarbons reacts with water and oxygen in order to form syngas, consisting of H_2 and CO, see Equation 1.1.

$$C_mH_n + m/2 \ H_2O + m/4 \ O_2 = mCO + (m + n/2) \ H_2 \tag{1.1}$$

In such fuel cell-ATR system, PHE's are very important for improving the efficiency. However, the environment in such system is very harsh due to the elevated temperature and high steam content of the gas. That, in combination with very small channels between the thin plates, makes the material selection very difficult. [4] Furthermore, sensitive catalysts are used in the ATR, meaning that it is very important to avoid formation of harmful compounds. Therefore, it is not possible to use chromia forming alloys for this application since it gives rise to evaporation of harmful chromium compounds.

2

Theory

In order to understand the results of this study, it is important to have some knowledge about the underlying theory of high temperature corrosion and the reason why to use an alloy instead of a pure metal when dealing with a corrosive environment.

2.1 High Temperature Oxidation

High temperature oxidation of a metal takes place when the material is exposed to an oxygen source in a high temperature environment. It is an electrochemical reaction where the atoms in the material and the oxygen forms an oxide scale at the surface of the substrate. If the reaction is rapid, and the oxide becomes thick and porous, it may lead to material failure. One way to reduce the oxidation rate is to alloy the metal with other elements such as aluminium or chromium. During oxidation, those elements will form optimally a thin, dense and slow growing oxide that prevents further reaction between the alloy and the oxygen.

In the following chapter, the general oxidation process will be described in terms of thermo-dynamics, types and growth mechanisms. The specific oxidation of FeCrAl-alloys will also be discussed.

2.1.1 Thermodynamics

If a reaction should be able to take place, it has to follow the thermodynamic exothermic trajectory. The second law, Equation 2.1, says that the Gibbs free energy, ΔG, of the system need to be negative in order to make a reaction thermodynamically spontaneous.

$$\Delta G = \Delta H - \Delta T S \tag{2.1}$$

H is the enthalpy, T is the temperature and S is the entropy. Further, the free energy

change can be expressed by using the equilibrium constant K_{eq} and the activities, a, of the reactants and products. For the oxidation of a metal, M, shown in Equation 2.2,

$$x\mathrm{M(s)} + (y/2)\mathrm{O_2(g)} \rightarrow \mathrm{M_xO_y(g)} \tag{2.2}$$

the free energy change can be described as

$$\Delta G = \Delta G^\circ + RT \ \ln K_{eq} = \Delta G^\circ + RT \ \ln \frac{a_{(\mathrm{M_xO_y})}(s)}{a_M^x(s) \ p_{O_2}^{y/2}(g)} \tag{2.3}$$

where ΔG° is the standard free energy of reaction and R is the ideal gas constant. Since the activities of pure solids can be set to unity and the one of a gaseous phase can be expressed as its partial pressure, following equation can be derived

$$\Delta G = \Delta G^\circ - RT \ \ln p_{O_2}^{y/2}(g) \tag{2.4}$$

where p_{O_2} is the partial pressure of oxygen. The above equation can be used to predict if the oxide or the corresponding metal will be stable in a specific temperature and environment. This is often visualized in the so called Ellingham diagram, shown in Figure 2.1. [9]
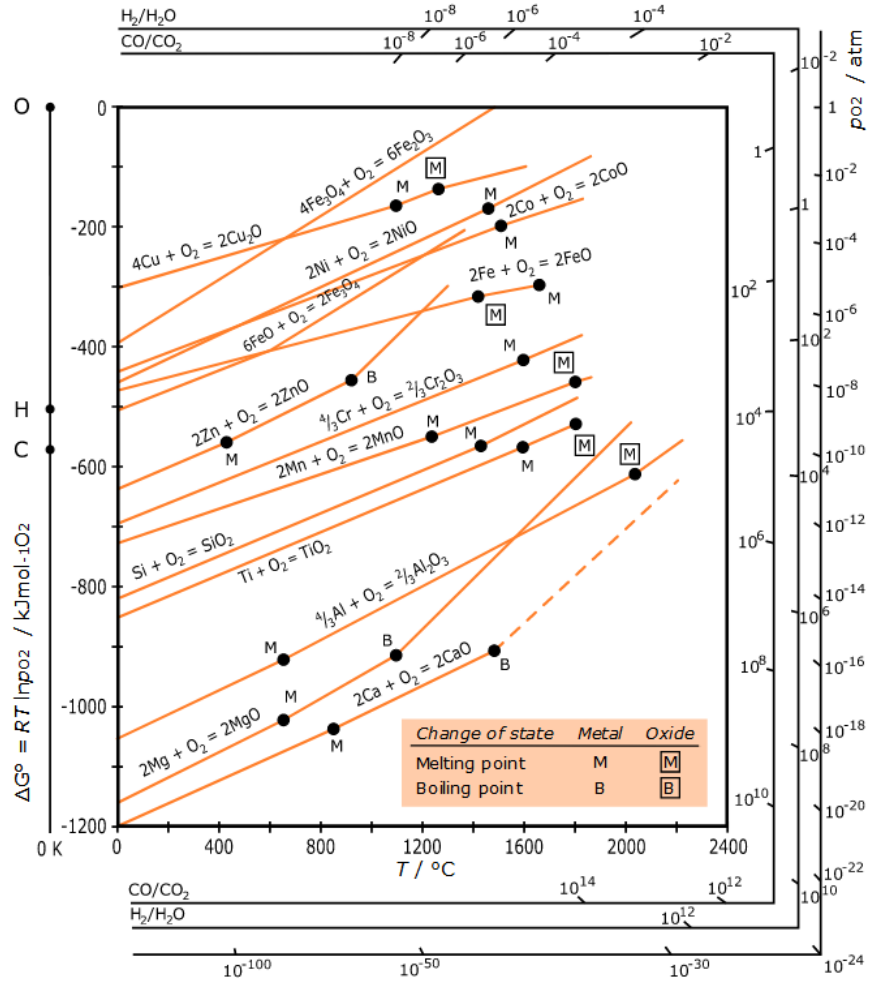
Figure 2.1: Ellingham diagram, showing the standard free energy versus temperature for selected oxides. [10]

By drawing a straight line from the "O" at the left hand side to the p_{O_2} of interest, as well as a vertical line from the present temperature, the potential oxidation of the metal can be predicted. If the lines intersect above the equilibrium line, the metal will oxidize. [11] In other words, if the partial pressure of O_2 is higher than the equilibrium partial pressure, the free energy change will be negative according to Equation 2.3. Consequently, the material will form an oxide layer at the metal-gas interface. [12]

2.1.2 Defects in Oxide Scale

Oxides can be divided into different categories based on their structure. The composition of a stoichiometric oxide, such as alumina, Al_2O_3, can be described by integers. If that is not the case, like for the iron oxide $Fe_{2-x}O_3$, the oxide is called a non-stoichiometric oxide. Defects,

needed for the oxide formation, are present for both groups, but the types are different. For stoichiometric oxides, Schotty and Frenkel defects are dominating. If an equal number of anions and cations are missing in the lattice, as shown in Figure 2.2a, it is categorized as Schotty defect. In such oxide, both anionic and cationic transport are possible. However, the oxide scale formation will be different depending on which ion that is mobile. If the anionic oxygen is transported from the gas phase towards the metal through the oxide, the growth of the oxide scale takes place at the metal-oxide interface and could therefore be called inwards growing oxide. Analogous, if the cationic metal ions are mobile, the oxide is outward growing since it grows at the oxide-gas interface. [13]

Frenkel defects describe the case where the anionic sub-lattice is complete, but the cationic sub-lattice contains vacancies. To maintain charge neutrality, cations are present as interstitial ions, see Figure 2.2b. Since metal ions alone are mobile, the oxide will grow at the scale-gas interface. [13]

Figure 2.2: Stoichiometric oxide defects: (a) Schotty defect (b) Frenkel defect.

A non-stoichiometric oxide do not have Schotty or Frenkel defect described above, but other point defects involving vacancies and interstitials. Non-stoichiometric oxides are semiconducting oxide, meaning that the anions in the lattice can variate their valence. The defects in such oxide may either be metal or oxygen excess or deficit. A so-called n-type semiconductor, where charges are transferred by negative carriers, is an oxide with either metal excess or non-metal deficit. Figure 2.3a shows the former case where metal ions are present as interstitials. To maintain the charge neutrality, there is an excess of electrons in the oxide. [14] The latter case, the non-metal deficit, has oxygen anion vacancies in the structure. Since the charge needs to be neutral, also this type of defect contains extra electrons and can therefore be classified as an n-type semiconductor. [13] The non-metal deficit oxide structure can be seen in Figure 2.3b.

Me^{2+}	O^{2-}	Me^{2+}	O^{2-}	Me^{2+}		Me^{2+}	O^{2-}	Me^{2+}	O^{2-}	Me^{2+}
O^{2-}	Me^{2+}	O^{2-}	Me^{2+}	O^{2-}		O^{2-}	Me^{2+}	O^{2-}	Me^{2+}	O^{2-}
	e^-							e^-		
Me^{2+}	O^{2-}	Me^{2+}	O^{2-}	Me^{2+}		Me^{2+}	O^{2-}	Me^{2+}	O^{2-}	Me^{2+}
		e^-		e^-					e^-	
O^{2-}	Me^{2+}	O^{2-}	Me^{2+}	O^{2-}		O^{2-}	Me^{2+}	[ ]	Me^{2+}	O^{2-}
	Me^{2+}									
Me^{2+}	O^{2-}	Me^{2+}	O^{2-}	Me^{2+}		Me^{2+}	O^{2-}	Me^{2+}	O^{2-}	Me^{2+}
			Me^+							
O^{2-}	Me^{2+}	O^{2-}	Me^{2+}	O^{2-}		O^{2-}	Me^{2+}	O^{2-}	Me^{2+}	O^{2-}

(a)   **(b)**

Figure 2.3: n-type semiconductors. (a) Metal excess, (b) non-metal deficit.

If the charge on the other hand is transferred by positive carriers, the oxide is referred to as a p-type semiconductor. As seen in Figure 2.4a, the p-type can be of metal deficit character with anionic vacancies. The charge change due to loss of cations are balanced by electron holes on other cations in lattice. Anions having the ability to be in several valence states, meaning having energetically close valence states, are typical positive semiconductors. [13, 14] The second type of positive semiconductor has an excess of interstitial oxygen anions and positive electronic defect, see Figure 2.4b. [14]

Me^{2+}	O^{2-}	Me^{2+}	O^{2-}	Me^{2+}		Me^{2+}	O^{2-}	Me^{3+}	O^{2-}	Me^{2+}
O^{2-}	Me^{3+}	O^{2-}	Me^{2+}	O^{2-}		O^{2-}	Me^{2+}	O^{2-}	Me^{2+}	O^{2-}
										O^{2-}
Me^{2+}	O^{2-}	Me^{2+}	O^{2-}	Me^{2+}		Me^{2+}	O^{2-}	Me^{2+}	O^{2-}	Me^{2+}
O^{2-}	[ ]	O^{2-}	Me^{2+}	O^{2-}		O^{2-}	Me^{2+}	O^{2-}	Me^{3+}	O^{2-}
Me^{3+}	O^{2-}	Me^{2+}	O^{2-}	Me^{2+}		Me^{2+}	O^{2-}	Me^{2+}	O^{2-}	Me^{2+}
O^{2-}	Me^{2+}	O^{2-}	Me^{2+}	O^{2-}		O^{2-}	Me^{2+}	O^{2-}	Me^{2+}	O^{2-}

(a)   **(b)**
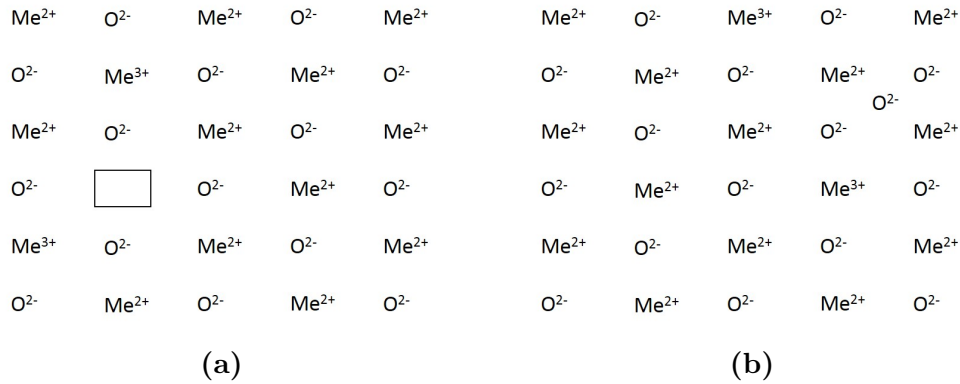
Figure 2.4: p-type semiconductors. (a) Metal deficit, (b) Non-metal excess.

The defects described above gives information about how ions and electrons can be transported within a crystal. But for some materials, the activation energy for such transport is very high, making this lattice diffusion kinetically impossible. This is the case for the non-conductive alumina oxide due to a large band gap. The growth of alumina is possible due to the grain boundaries where ions are allowed to move more freely. [13] If the surfaces of the grains are hydroxylated, also the electrical conductivity of the oxide is improved. [15]

2.1.3 Kinetics

The oxidation process starts when oxygen reaches the surface of a metallic material. The oxygen is adsorbed and reduced into O^{2-} ions with e^- from the metal and form together with metal cations oxide nucleation points. With time, the oxide grows thicker and covers the whole surface. From here on the conductivity of the oxide becomes decisive. The oxidation course is illustrated in Figure 2.5.
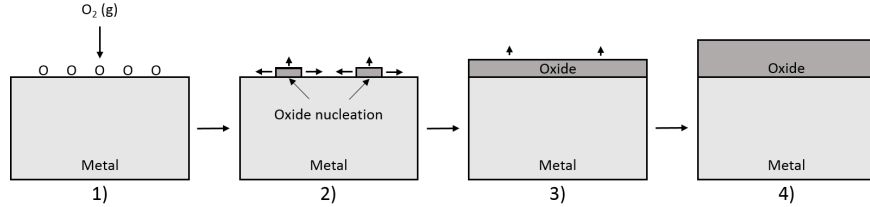
Figure 2.5: Illustration of the oxide formation from a metal surface. 1) adsorption of O_2, 2) oxide nucleation, 3) continuous oxide growth and 4) oxide grows thick.

When the metal oxidise, the mass of it increases due to incorporation of oxygen. Figure 2.6 shows three different mass gain curves that are used to describe oxidation processes: the linear, parabolic and logarithmic rate oxidation.
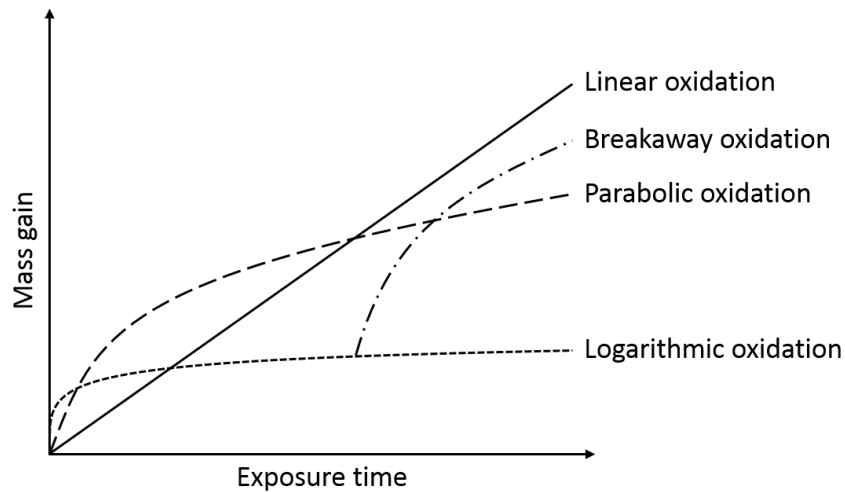
Figure 2.6: Kinetic rate laws for oxidation of metal and breakaway oxidation.

There are mainly two mechanisms that affect the oxidation rate, the transfer of oxygen from the gas bulk to the surface and the diffusion of ions and electrons within the scale. In the initial part of the oxidation, the diffusion through the scale is rapid, leading to that the oxygen supply from the atmosphere to the interface is the rate determining mechanism. The

oxidation rate of such system can be described by the linear rate law, shown in Equation 2.5,

$$x = k_l \, t \tag{2.5}$$

where k_l is the linear rate constant. Except for the initial oxidation, the linear rate law may also be used to describe the scale growth of highly porous oxides where the gas has the ability to be transferred within pores. [11]

If, however, the oxide is compact without a large fraction of pores, the thickness of scale affects the oxidation rate as the oxidation reaction proceeds. When the oxide scale grows and becomes thicker, the diffusion rate of ions and e^- within the scale decreases. Thus, the linear rate law is not valid anymore. Instead, the process can be described by e.g.the parabolic rate equation.

$$x^2 = 2k_p \, t + C \tag{2.6}$$

Where k_p is the parabolic rate constant and C is a constant. As can be seen in Figure 2.6 the weight gain, and therefore also the thickness of the oxide scale, increases rapidly during the first part of the oxidation of the parabolic curve. When the oxide grows thicker, the ion and charge transport paths within the scale becomes longer, leading to that the rate of e^- supply to the oxidising surface decreases. [16] Consequently, the mass gain rate decreases. The parabolic rate law can often be used to describe the growth of a thin, adherent and protective oxide scale.

A third equation that can be used to describe the oxidation mechanism of a metal is the logarithmic rate law, shown in Equation 2.7

$$x = k_{log} \, log(t + t_0) + A \tag{2.7}$$

k_{log} is the logarithmic rate constant and A is a constant. This equation is commonly used to describe the oxidation of metal at relatively low temperatures when a protective oxide film is rapidly formed in the very initial part of the process. [2] The logarithmic rate law is just one of many models describing the so called sub-parabolic oxidation process, where the mass gain curve lies below the one of the parabolic rate.

Figure 2.6 also shows a phenomena called breakaway oxidation. That is when the mass gain increases drastically after a period of time. That happens if the protective oxide is damaged due to harsh environment. When the protective layer is gone, fast growing oxidation products are formed at the surface. This leads to break down of the material.

2.1.4 Chromium Evaporation

When metals or alloys are exposed to high temperature, oxidation is not the only reaction occurring. For chromium containing alloys oxidising in wet atmosphere, also chromium evaporation from the oxide must be taken into consideration. Chromium(III) oxide, called chromia, reacts with O_2 and H_2O to form the volatile gas $CrO_2(OH)_2$ as seen in Equation 2.8 and in Figure 2.7. [17] If the temperature is high enough, above 1000°C, chromium evaporation from the oxide is possible even if water is not present. [9]

$$1/2 \ Cr_2O_3 \ (s) + 3/4 \ O_2 \ (g) + H_2O \ (g) \Leftrightarrow CrO_2(OH)_2 \ (g) \tag{2.8}$$
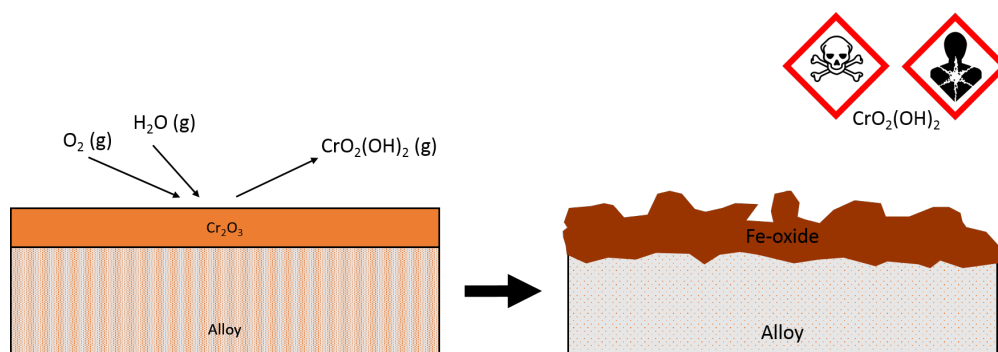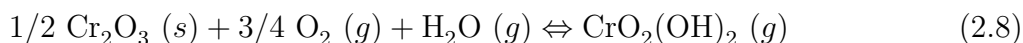
Figure 2.7: Chromia evaporation from oxide in presence of H_2O.

Chromium evaporation is a devastating problem seen from different perspectives. First, the evaporation exhausts the protective oxide of chromium, meaning that the oxide rate increases in order to maintain the protective oxide. This may however lead to chromium depletion of the alloy that could cause severe corrosion problems and even material break down. Second, in the case of the fuel cell application, the evaporated hexavalent compound leads to poisoning of the catalyst in the ATR. Furthermore, $CrO_2(OH)_2$ is carcinogenic and should therefore not be released uncontrolled. [18]

2.2 FeCrAl Alloys

The so-called FeCrAl alloys are iron based alloys containing aluminium and chromium together with small amounts of other elements. Since this group of alloys forms the protective alumina oxide, Al_2O_3, at high temperature under oxidising conditions, they are well used for thermal processes up to 1250°C. The Al- and Cr- content in FeCrAl-alloys usually lay between 3-6 wt% and 5-15 wt% respectively. The oxidation resistance increases with Al-content, but unfortunately, the mechanical properties of the material are impaired. The alloy becomes

brittle and the workability and weldability decreases with increasing Al-content. [3], [2] By adding Cr to the alloy, the amount of Al needed to form a protective oxide scale can be lowered, due to the so-called third element effect (TEE). [19],[16] However, if the Cr-content is high, the risk of Cr-evaporation increases. Consequently, a good alloy for the purpose should contain the lowest possible amount of Al and Cr, but still enough to form a protective oxide scale.

Al_2O_3 exists in different crystal phases, of which α-Al_2O_3 is the most stable. Since α-Al_2O_3 is dense, continuous and slow growing, due to its low conductivity, the oxide forms a protective scale and therefore prevents break down of the material. α-Al_2O_3 is the dominating phase at 1 000°C or higher. [20]

At lower temperatures, the nucleation of the α-Al_2O_3 is slow and so-called transient phases, such as γ-, κ- and δ-Al_2O_3, as well as mixed oxides, tend to form instead. [20],[2] The transient oxides are less dense and thus not as protective as the α-Al_2O_3. However, the transient Al_2O_3 are thermodynamically metastable and will therefore transform into α-Al_2O_3 given time. The temperature at which the transformation takes place has been discussed, traditionally the transformation temperature is said to be around 1 000°C. [20] Studies performed at lower tempertatures are scarce, but by the use of XRD, it has been proven that α-Al_2O_3 might exist at temperatures as low as 700°C. [2] However, a lower temperature means that the potential transformation to α-Al_2O_3 takes longer time.

It has also been shown that water vapour affects the oxidation of FeCrAl-alloys by increasing the oxidation rate in the beginning of the oxidation. Liu et al. (2005) [21] reported that when a FeCrAl alloy was exposed at 900°C in O_2 containing 40% H_2O, the oxidation rate was significant higher compared with the same exposure performed in dry O_2. In another paper they reported that water vapour stabilises the γ-Al_2O_3. [22]

2.2.1   Growth of Al_2O_3 from FeCrAl Alloy

The formation of an oxide scale on an alloy, in this case a FeCrAl alloy, is more complex than the oxide formation from a pure metal. The compound's reactivity and oxygen affinity are examples of properties that affect the oxidation. Liu et al. (2007) [21], who studied the oxide formation of FeCrAl alloys at 900°C, divided the oxide growth and transformation into four stages. Figure 2.8 and following list explain the formation.
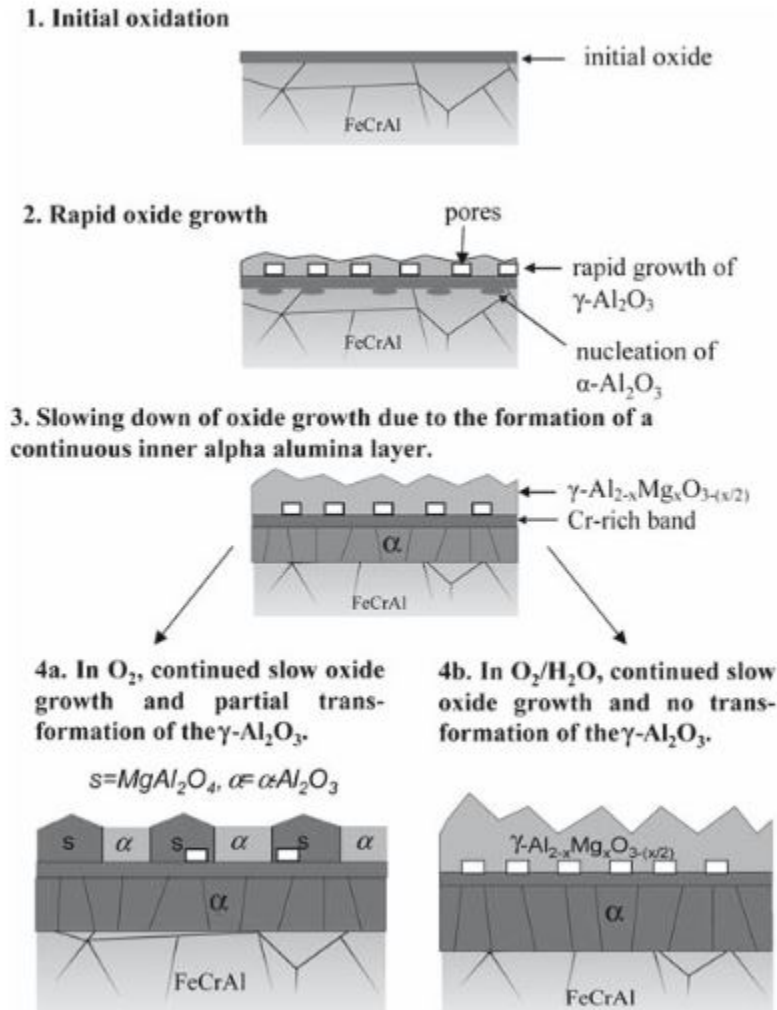
Figure 2.8: Schematic illustration of the formation of γ-Al$_2$O$_3$ at a FeCrAl alloy in dry O$_2$ and O$_2$ with H$_2$O vapour. [21]

1. In the initial part of the oxidation, a corundum-type mixed oxide and γ-Al$_2$O$_3$ nucleate at the surface of the alloy.

2. As the oxidation proceeds, there is a rapid outward growth of γ-Al$_2$O$_3$. The nucleation of initial mixed oxide remains as a Cr-rich band, positioned at the original alloy surface. Pores formed in the outward growing oxide can also be found in this region. The γ-Al$_2$O$_3$ layer will be enriched with Mg and Fe since the oxide provides outward transport of those ions. Furthermore, α-Al$_2$O$_3$ nucleates from the initial oxide and grows slowly inwards.

3. When the inwards growing α-Al$_2$O$_3$ forms a continuous scale, the growth rate of the outer γ-Al$_2$O$_3$ decreases due to limited supply of cations through the inner layer.

4a. In dry O$_2$, the outer oxide partly transforms to α-Al$_2$O$_3$ and continues the outward

growth with a slow rate. The outer scale also consists of γ-$Al_{2-x}(Mg,Fe)_xO_{3-(x-2)}$ and $(Mg,Fe)Al_2O_3$, Where the former transforms into Mg,Al_2O_4 and α-Al_2O_3.

4b. In wet atmosphere, the transformation of the layers differ. The protective α-Al_2O_3 will exclusively be found in the inner layer. The outer layer consists of γ-$Al_{2-x}(Mg,Fe)_xO_{3-(x-2)}$ since water vapour stabilises the transient phase, consequently, no transformation is possible. [21]

Engkvist et al. (2009) [23] showed that the formation of oxide from FeCrAl alloy differs when the temperature is decreased. In addition to lower oxidation rates at lower temperatures, it was shown that the composition of the oxide was different when the alloy was exposed at 500°C and 700°C. At 700°C, the Cr-rich band observed at 900°C was still present, separating the inward growing α-Al_2O_3 from the outward growing γ-Al_2O_3. However, the oxide contained a higher amount of both Cr and Fe compared to the 900°C exposure. When the temperature was decreased to 500°C, the oxide scale was completely different. Instead of the two distinct alumina scales and Cr-band, the oxide was a mixture consisting of Al, Cr and Fe. The study was performed in both dry air and in air humidified with 40% water. At 900 °C, the result was the same as Liu et al (2007) had shown, but at 500°C and 700°C, the mass gain and oxide composition were similar in dry and wet exposures. Also the mass gains were similar, regardless of if water was present or not, at the two lower temperatures, at 900°C, the wet exposure gave rise to a higher mass gain. [23]

2.2.2   Reactive Elements and Si in FeCrAl Alloys

As mentioned earlier, the amount of Al and Cr should be low not to risk the mechanical properties of the material to deteriorate. To make sure that the oxidation behaviour is good enough, so-called reactive elements (RE), such as Zr, Ti or Y, can be added to the alloy. When such elements are used in an alloy containing aluminium, the adhesion of the alumina scale at the alloy substrate will be improved. [2] Why RE improve the adhesion has been studied for a long time. One reason could be the growth of oxide covered pegs, acting as anchors for the oxide. [20] Another hypothesis is that the addition of RE changes the mechanism of oxide growth and transport processes within the oxide, leading to less stresses and therefore increased adhesion of the oxide to the surface.

In a recent study by Mortazavi et al (2018) [24] the interplay of water and RE has been investigated. It was concluded that RE particles in alumina forming alloys enable water to penetrate the oxide layer via hydroxylated and RE-ion decorated grain boundaries in the oxide. Since it is not possible to transport ions or electrons through alumina crystals, [13] the now open transport paths lower the energy for transport leading to faster oxidation. When the RE-ions are consumed, grain coarsening sets in since nothing holds the grain boundaries open. When the density of transport paths decreases, also the oxidation rate decreases to a sub-parabolic behaviour. [20],[24]

In addition to RE FeCrAl alloys may also contain a small amount of Si in order to improve the corrosion resistance. Eklund et al (2018) [25] used alloys with 10% Cr, 4% Al and 0, 1 or 2% Si in order to investigate the Si effect. It was shown that an addition of just 1 wt% Si was enough to decrease the mass gain from 10 to 0.03 mg/cm$_2$ when samples were exposed in O$_2$ and 20% H$_2$O for 168 hours at 600°C. [25]

Except for the work performed by Eklund, research investigating the effect of Si in FeCrAls are scarce. A study by Chęcmanowski et al. (2013) [26] showed however that the corrosion resistance was improved if the alloy was coated with a silica and alumina containing coating. It was shown that aluminsilicates, e.g. mullites, were formed in the oxide during high temperature oxidation. [26]

3

Experimental

3.1 Materials

Two different FeCrAl alloys from the Swedish steel company Kanthal were exposed, analysed and compared. The alloys were produced by casting and hot rolling into sheets before they were annealed. The first alloy used is a commercial high temperature alloy named Alkrothal™, in this work referred to as A14. The chemical composition can be seen in Table 3.1.

C wt%	Al wt%	Cr wt%	Mn wt%	Si wt%	Fe wt%	Other
0.03	4.35	14.8	0.22	0.33	Bal.	RE-elements

Table 3.1: Chemical composition of Alloy A14.

The second alloy, referred to as A197, is a model alloy. The nominal chemical composition of this alloy is shown in Table 3.2. Compared with A14, this alloy contains less Cr and Al but more Si. Like A14, this alloy contains small amount of reactive elements.

C wt%	Al wt%	Cr wt%	Mn wt%	Si wt%	Ni%	Fe wt%	Other
<0.08	3.2-4.2	11-14	<0.7	1-2	0.5	Bal.	RE-elements

Table 3.2: Chemical composition of Alloy A197.

3.1.1 Experimental Chart

The two alloys were exposed at two temperatures, 600°C and 800°C, in both dry air and air containing 40% water vapour for 20 or 200 hours. In total, 16 exposures have been performed. The exposures are summarised in Figure 3.1.

Figure 3.1: Table showing the temperatures, alloys, conditions and times used for the exposures.

3.1.2 Sample Preparation

A14 and A197 coupons of dimensions 12x12x1 mm were ground with SiC paper to 4000 grit before polished with 1 μm diamond paste in order to obtain a mirror like finish. The edges of the coupons were ground by 1000 mesh paper only. The coupons were then cleaned with water, acetone and ethanol using an ultrasonic bath at room temperature. Figure 3.2 shows SEM images of A197 and A14 after preparation but before any exposure.

(a) A197   (b) A14
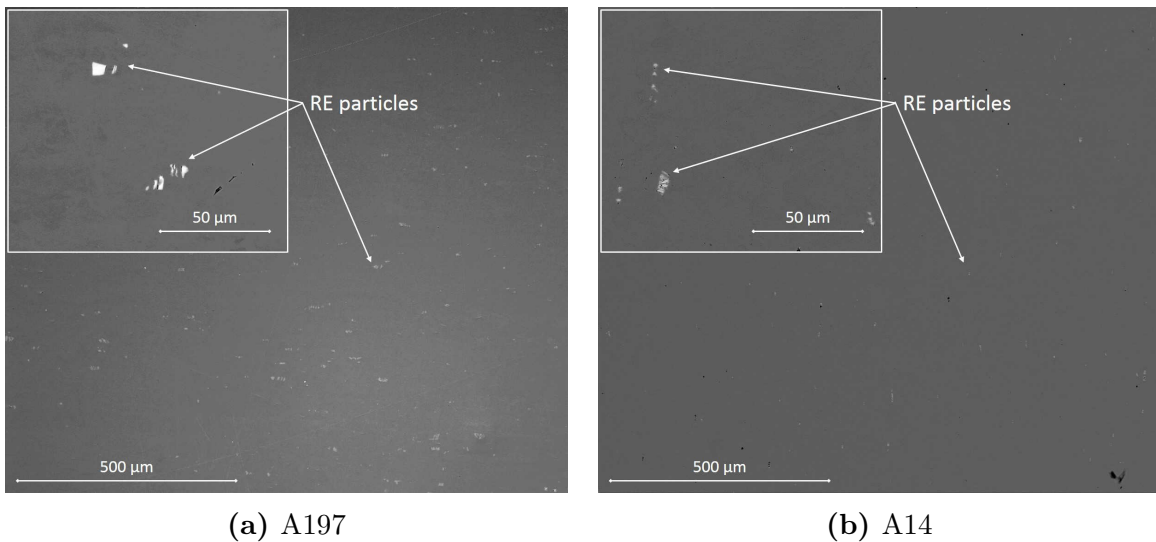
Figure 3.2: BSE images of polished A197 and A14.

3.2 Experimental Setup

Since it was of highest importance to make sure that the evaporation of chromium was low, in order to not poison the fuel cell, a special experimental set up called "Denuder technique" was used. The technique, which has been developed and used at Chalmers for a long period of time, has many advantages. For example, it is possible to collect and quantify the chromium evaporation from the samples at different time periods, without disrupting the isothermal

exposure. The method has shown good results in several studies. [9, 17]

For each exposure, three coupons were prepared as described in previous section and placed in a sample holder located in a horizontal tubular quartz reactor, as shown in Figure 3.3. The reactor was inserted in a furnace where air, dry or moisturised with steam, were lead to the inner tube through a flow restrictor in order to ensure a uniform gas flow. At the other end of the inner tube, a denuder, which is a thin Na_2CO_3 coated quartz tube, was inserted. When steam was used, the water vapour reacted with the oxide and gave rise to chromium evaporation, as described in section 2.1.4. The volatile compound was carried by the gas into the denuder where a reaction with the Na_2CO_3 coating took place, see Equation (3.1). In this way, the Chromium was caught in the denuder.

$$CrO_2(OH)_2(g) + Na_2CO_3(s) \rightarrow Na_2CrO_4(s) + CO_2(g) \tag{3.1}$$
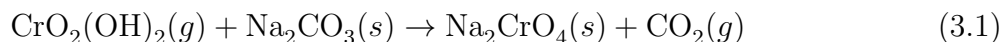
The gas mixture was then lead to a wash bottle where unreacted $CrO_2(OH)_2$ was dissolved in water. To ensure that the entire gas flow was flowing through the denuder, the quartz reactor was sealed with an end cap. The tube was insulated with a heating cord and aluminium foil in order to prevent condensation. After the exposure, the Cr containing coating in the denuder was dissolved in a predetermined amount of water. UV/Vis (Evolution 60S UV-visible spectrophotometer, wavelength of 370 nm) and a calibration curve (range: Abs 0.2 to 1.6) were used in order to calculate the amount of Cr evaporated from the sample.

In this work, dry air and air containing 40 vol% water vapour were used. The water content was controlled by bubbling the gas through a water bath before it was lead through a condenser with temperature set to reach the wanted water vapour content.
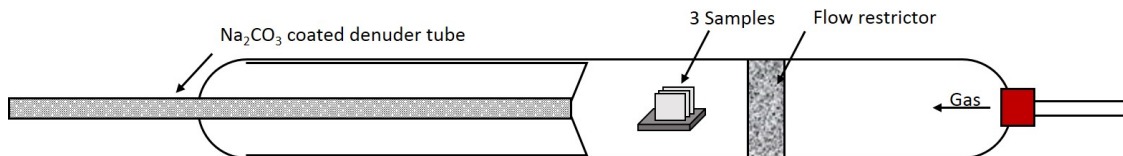
Figure 3.3: Schematic drawing of experimental set up.

3.2.1 Experimental Procedure

In order to get comparable results, all experiments were carried out by the same experimental protocol. A description of the protocol can be found in Appendix 1.

3.2.2 A14 Field Experiment

A field experiment was performed in order to investigate the corrosion resistance of A14. A coupon of the alloy was placed, by the staff at PowerCell, in a reformer running for 90 hours at a temperature around 600°C and water content similar to lab exposures.

3.3 Characterisation Techniques

Several characterisation techniques were used in order to investigate the oxidation products. In following section, SEM, EDX, XRD and TEM are described.

3.3.1 Scanning Electron Microscopy

Scanning Electron Microscopy (SEM) can be used to investigate the surface morphology and chemical composition of a sample. In such an instrument, an electron beam is focused on the sample and follows a raster providing an image. Depending on if the image has been provided by the detection of secondary electrons (SE) or backscattered electrons (BSE) from the sample, different information can be obtained from the image. Since SE originates from atoms very close to the surface it is possible to use SE images in order to investigate the surface morphology of the sample. BSE, emitted from a larger depth, gives information about the chemical composition of the sample. [27, 28, 29] The interaction depth is illustrated in Figure 3.4.

The electron beam also gives rise to X-ray radiation from the sample. [29] The X-rays can be analysed by Energy Dispersive X-Ray Spectroscopy (EDX) in order to obtain even more advanced information regarding the chemical composition. However, the resolution of the obtained images are comparatively low due to the fact that the interaction volume is much larger than the ones of both secondary and backscattered electrons. [16] The advantage is that quantitative studies of the sample can be performed. By changing the voltage of the electron beam, the volume of interaction can be adjusted. The higher the voltage, the larger the interaction volume, but the interaction volume is also material specific.
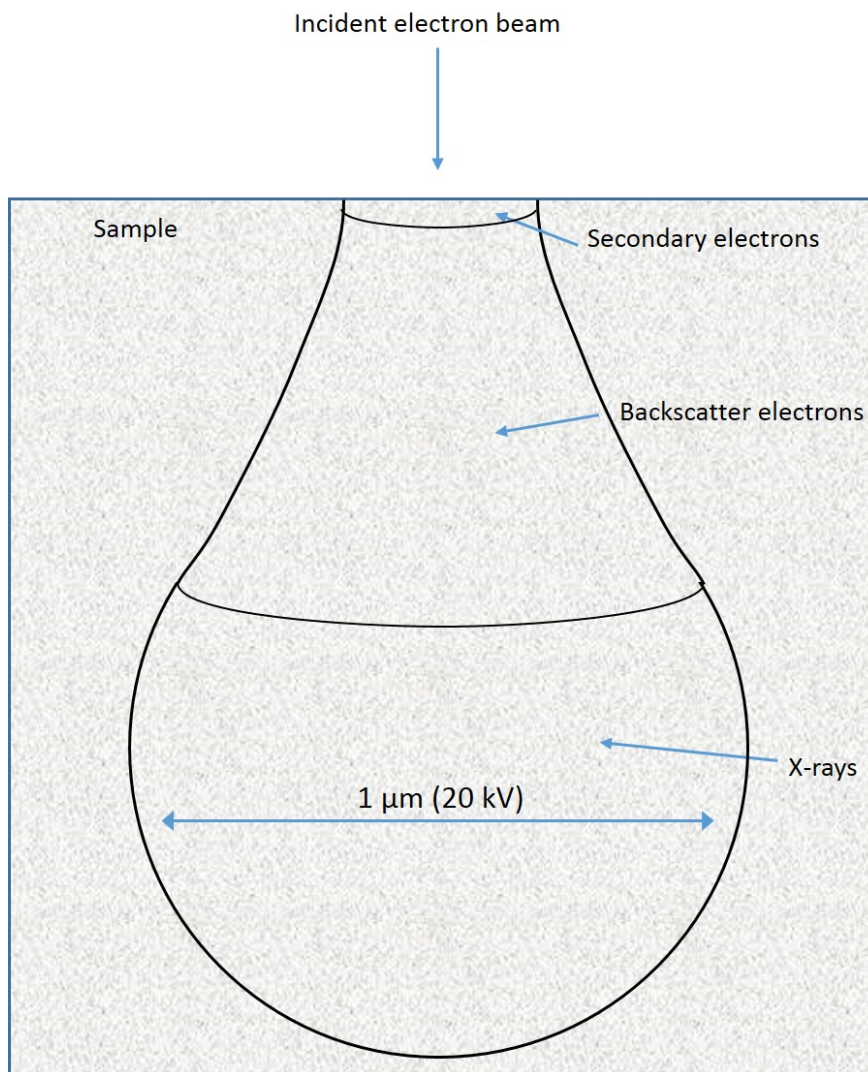
Figure 3.4: Interaction volume for generation of secondary electrons, backscattered electrons and x-ray radiation. The interaction volume is material dependent.

Two different SEMs were used in this project: Quanta 200 ESEM from Thermo Fischer Scientific and Ultra 55 FEG from Zeiss. The former was used for plan view investigations of oxides. A voltage of 5 to 20 kV and the spot size 3 was used. The working distance was around 10 mm. The EDX software INCA was used to obtain information about the chemical composition.

Due to very thin oxide scales, the resolution of the comparatively large beam diameter found in the Quanta 200 ESEM instrument was not enough to study cross-sections of the oxides. For that purpose, Ultra 55 FEG SEM was used. This SEM, provided with an in-lense detector, was used with the low accelerating voltage of 2 kV and a short working distance of just 2 mm. With those settings, it was possible to obtain images with very high magnification. Samples for cross-sectional examination were prepared by gold- or platinum

sputtering in order to make the oxide conductive. A silicon wafer was glued to the surface and the sample was cut in half. To obtain a smooth cross-section surface, Broad Ion Beam (BIB) milling was used. The instrument consists of one or several ion sources, in this case gallium, and a vacuum chamber, in which the cut sample is placed. Heavy ions are bombarding the sample upon atoms are sputtered from the surface of the sample. To prevent uncontrolled sputtering, a mask protects the most of the sample except for the area where the milling should be performed. The BIB instrument Leica TIC3X was used in this project. The voltage was set at 8 kV and the instrument was milling for 4 hours.

3.3.2   X-Ray Diffraction

X-ray Diffraction (XRD) is an analysis method that is able to identify the structures within a crystalline sample. This feature is of high importance when investigating for example Al_2O_3, since the oxide can exist as both α-Al_2O_3 and transient phases such as γ- and β-Al_2O_3.

In a perfect crystalline material, the lattice atoms are arranged in a periodic pattern with planes separated by the same distance. During X-ray diffraction, the sample is in focus of monochromatic X-rays. When the incident beam are diffracted by the periodic material, a diffraction pattern occur if the X-rays are in phase and interfere constructively. This is described by Bragg's law [13, 29]

$$n\lambda = 2d_{hkl} \sin \theta \qquad (3.2)$$

Where λ is the wavelength of the X-ray, d_{hkl} the lattice plane spacing and θ_{hkl} the angle between the incoming X-rays and the sample. In order to fulfil Bragg's law, n needs to be an integer. A schematic drawing explaining Bragg's law can be seen in Figure 3.5. [13]
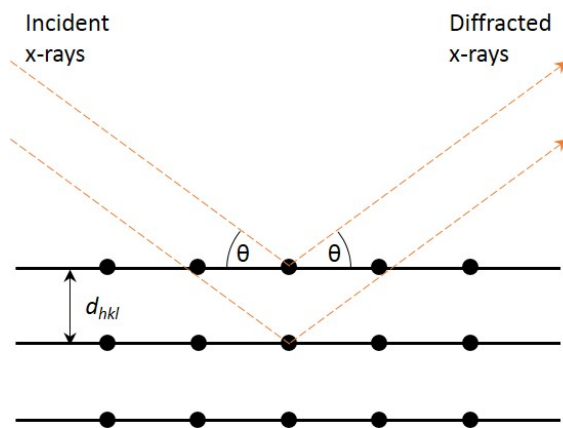
Figure 3.5: Schematic drawing of Bragg's law.

In this study, the XRD patterns were detected using grazing incidence beam. The samples were scanned over the angular range $10°\ \leq 2\theta \leq 90°$. The incidence angle was 0.2°or 5°, depending on the purpose of the scanning. A smaller angle is preferred when an oxide in the nm scale is to be investigated, while a larger angle gives more information about the bulk material.

3.3.3   Transmission Electron Microscope

Since the chemical composition was expected to differ throughout the oxide scales, depth-profiling was performed by Scanning Transmission Electron Microscopy (STEM). In STEM, the electrons are transmitted through the sample, and not scattered back as in SEM. With STEM, the chemical composition, crystal structures and morphology of the sample can be studied in detail. [13] FEI Titan 80-300 TEM was used in this project.

To prepare the specimen for STEM, Focused Ion Beam (FIB) was used. The instrument can be compared with a SEM since both operate in a similar way. The main difference is that FIB do not only use an electron probe, but also an ion probe bombarding the sample with ions. When the ions interact with the surface, the atoms are sputtered away. Therefore, FIB can be used as an atom mill. [20] By continuous milling, it is possible to create a lift-out of a region of interest for further investigation by STEM and SEM-EDX. Since the lift-out is a very thin foil, the electron beam is transmitted through the sample, leading to that the sample can be investigated even if the accelerating voltage is low. This is shown in Figure 3.6.

To avoid damages of the lift-out itself, a protective layer of Pt is deposited before the milling. The FIB instrument FEI Versa 3D was used for the lift-out preparations. The STEM and FIB work were performed by Vijayshankar Asokan.
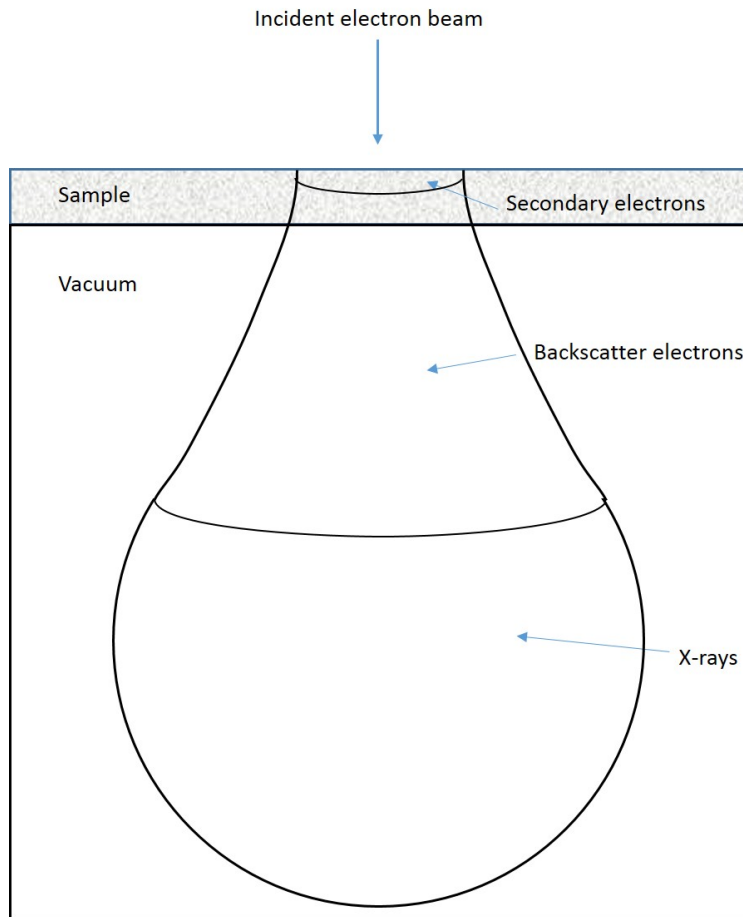
Figure 3.6: Interaction volume of electron beam when investigating a thin foil.

4

Results

The result part of this thesis consists of mass gains of coupons due to oxidation, chromium evaporation data, images and data from SEM, EDX and STEM and XRD. The result is divided into two main sections, depending on exposure temperature used.

4.1 Exposures at 800°C

In following sections, the results from the 800°C exposures are presented. The result consists of evaporation data, mass gains, images obtained from SEM and EDX together with STEM investigation of the oxides.

4.1.1 $CrO_2(OH)_2$ Evaporation and Mass Change
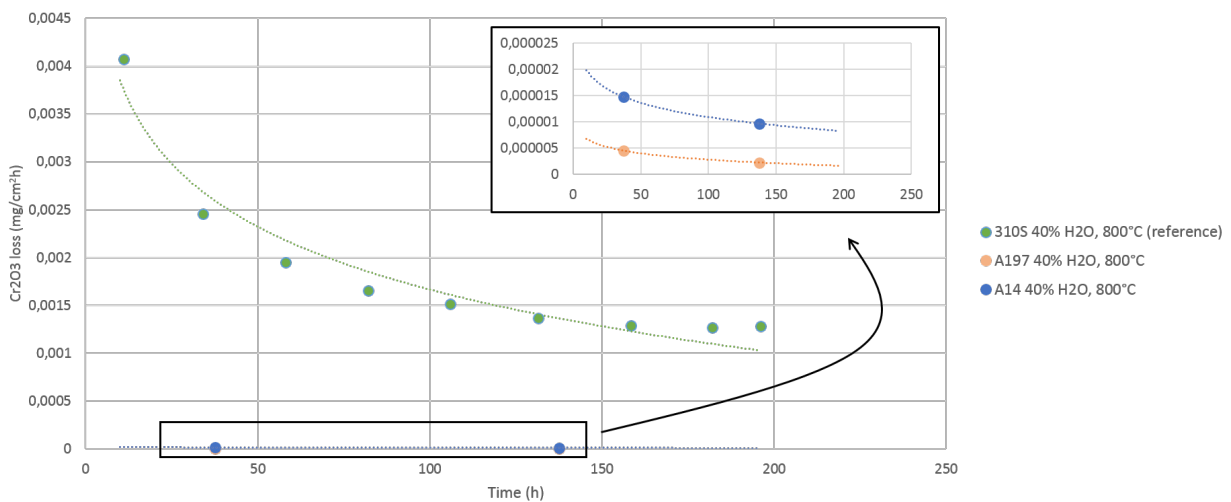
Figure 4.1: Chromia evaporation rate measured for A14, A197 and 310S exposed at 800°C in air containing 40% water vapour, together with logarithmic trendlines.

The amount of $CrO_2(OH)_2$ evaporated from the oxide was measured by UV/Vis spectrometry. Figure 4.1 shows the evaporation rate from the alloys exposed at 800°C, together with a reference alloy, named 310S containing 25 wt% Cr and 20 wt% Ni. While A197 and A14 form alumina, 310S is a common chromia forming stainless steel used for high temperature applications. [30] Since water is needed for the evaporation, the figure only shows data from the wet and not the dry exposures. The concentration of detected chromium compound from A197 and A14 was even lower than the lowest value used in the calibration curve, meaning that there could be some uncertainties regarding the exact values.
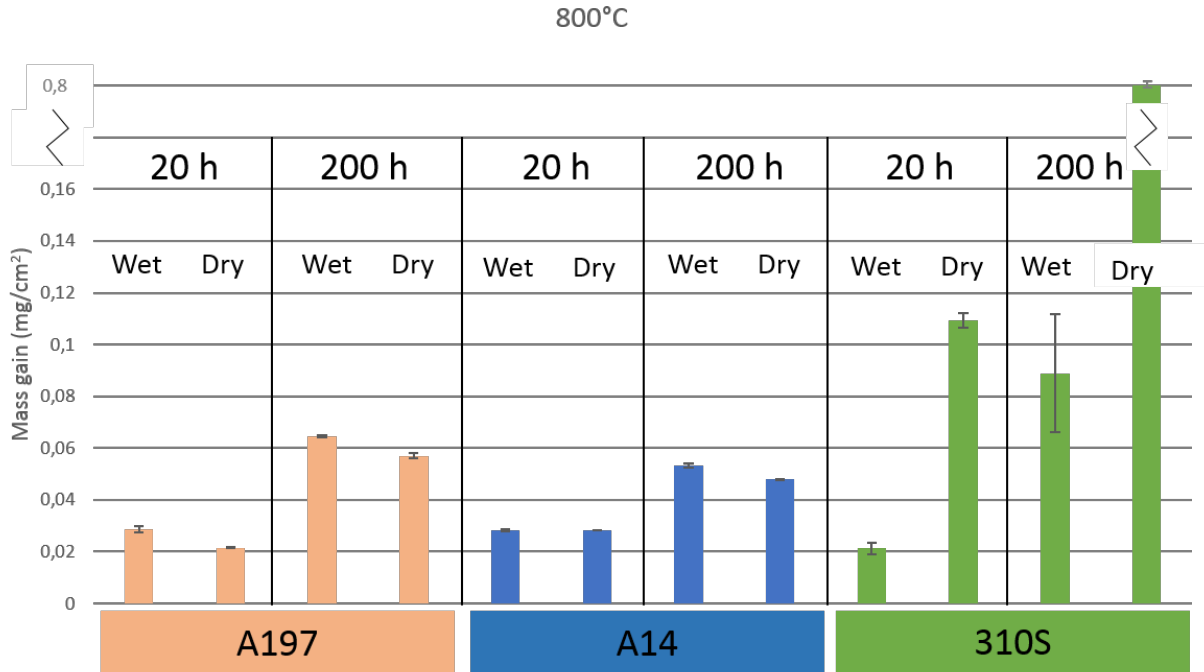
Figure 4.2: Mass gain due to oxidation of alloys A14, A197 and 310S in dry air and air containing 40% H_2O at 800°C.

The mass gains of A14, A197 and the reference alloy 310S exposed in dry air and in air containing 40% water vapour at 800°C are shown in Figure 4.2. Since the mass gain correlates to the oxide scale thickness, the thickest oxide of the two alumina forming alloys is expected to be found for A197 exposed for 200 hours in wet atmosphere. Both alloys investigated in this thesis show a lower mass gain when exposed in dry air. However, the difference in mass gain between the dry and wet atmosphere seems to be lower in the case of A14. Since the chromia forming 310S alloy evaporates Cr in wet environment, the net mass gain is highest in dry condition.

The reference alloy 310S is a chromia and not an alumina forming alloy, hence the data looks

different. Since chomia evaporates in water containing environment, the net mass gain is underestimated for the wet exposures.

4.1.2   Plan View Investigation of the Oxides

The morphology and chemical composition of the oxides formed from the alloys were investigated by SEM. Both BSE and SE were used. The BSE images of the four different exposures of A197 at 800°C are shown in Figure 4.3. All the samples are fully covered by a smooth, thin base oxide, while the RE particles are covered by thicker oxide. Element mapping performed via EDX-data indicated that the thicker oxide was Al_2O_3 based. This effect was most significant in the 200 hours exposure of A197 in wet atmosphere, see Figure 4.4. Furthermore, a "halo" with less aluminium was found around each RE particle from this specific exposure. The effect was not found after dry exposures.
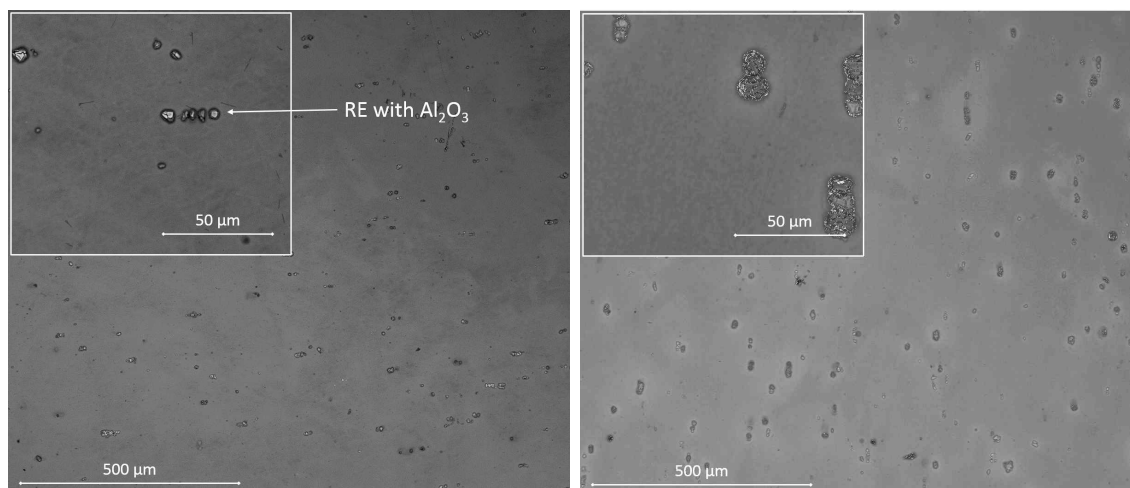
(a) A197, 20 h, 40% H_2O, 800°C.

(b) A197, 200 h, 40% H_2O, 800°C.
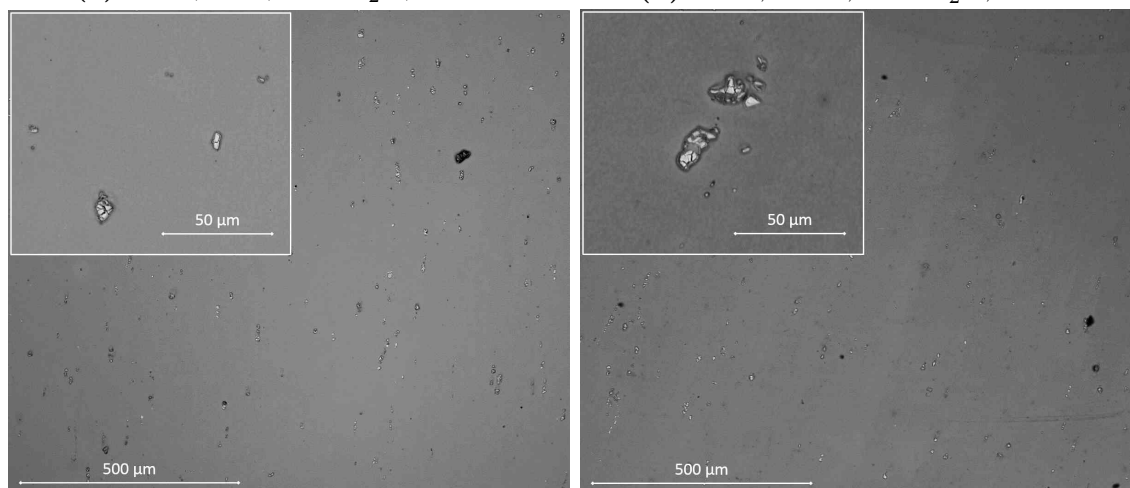
(c) A197, 20 h, dry air, 800°C.

(d) A197, 200 h, dry air, 800°C.

Figure 4.3: BSE images of A197 exposed at 800°C
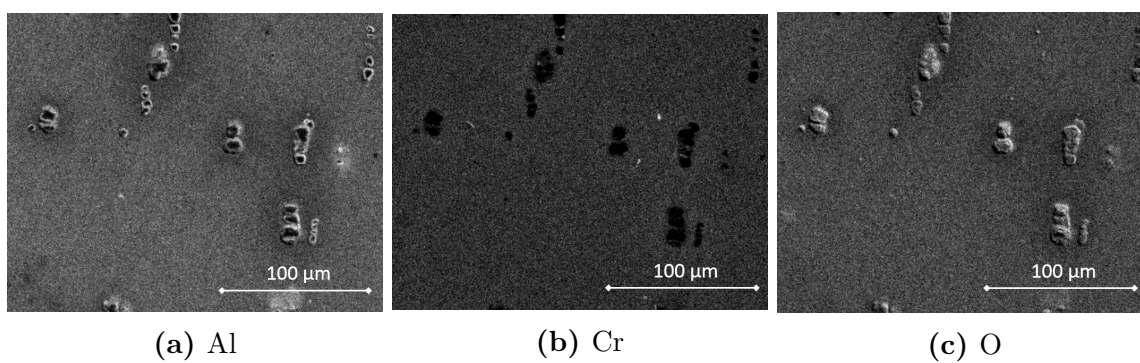
(a) Al

(b) Cr

(c) O

Figure 4.4: EDX mapping of A197 exposed in air with 40% H_2O at 800°C. Bright areas indicate locations with a higher concentration of respective element.

The BSE images obtained from A14 exposed at 800°C are shown in Figure 4.5. The grains are easily seen, as well as oxidation at the grain boundaries. The RE particles have some amount of thicker alumina, but not as pronounced as the particles in A197. The RE-particle density is also much lower in the case of A14.

(a) A14, 20 h, 40% H_2O, 800°C.

(b) A14, 200 h, 40% H_2O, 800°C.

(c) A14, 20 h, dry air, 800°C.

(d) A197, 200 h, dry air, 800°C.
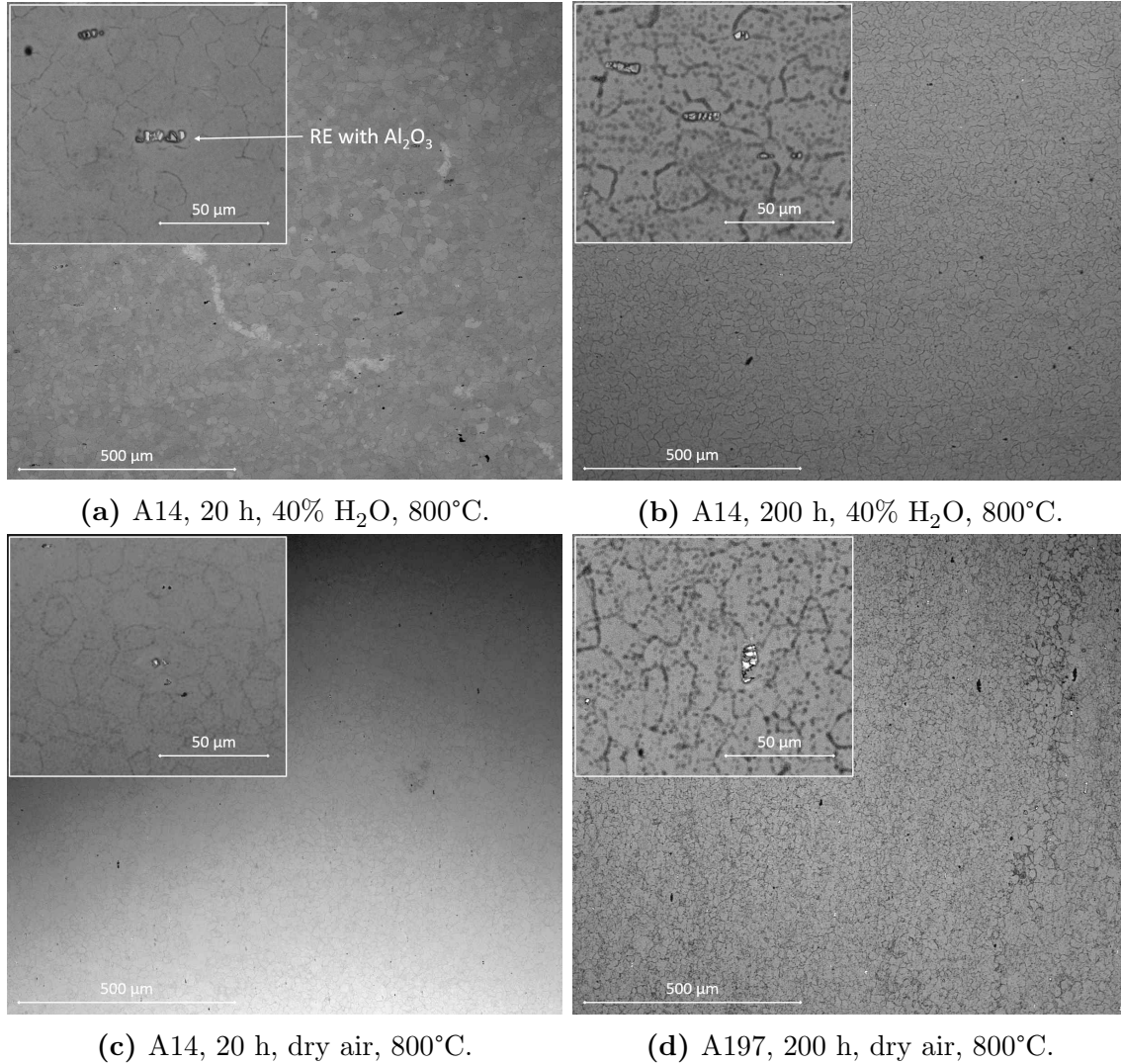
Figure 4.5: BSE images of A14 exposed at 800°C.

(a) RE   **(b)** Al   **(c)** Cr
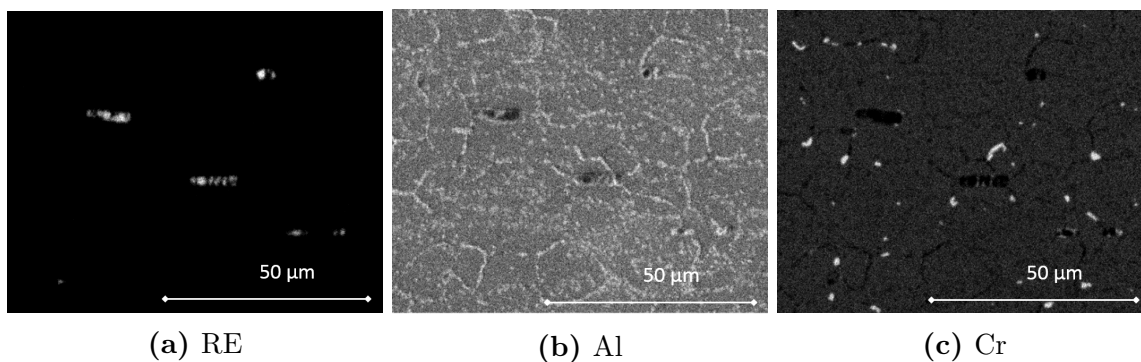
Figure 4.6: EDX mapping of A14 exposed in air with 40% H_2O for 200 hours at 800°C. Bright areas indicate locations with a higher concentration of respective element.

4.1.3 Cross-Section Investigation of the Oxides

The thickness and morphology of the oxides were investigated by SEM analysis of sample cross-sections. Figure 4.7 shows the results from the 20 and 200 hours exposure of A197 in wet atmosphere at 800°C and Figure 4.8 shows the 20 hours exposure of the same alloy and temperature, but in dry air. The former figure shows that the oxide is relatively smooth and has a thickness of about 200 nm. After 200 hours, the thickness has increased to about the double. The oxide is not homogeneous since a higher number of void-like shapes can be found in the oxide closer to the oxide/alloy interface. Furthermore, some brighter shapes can be observed from the cross-section images in the outer part of the oxide. The alloy exposed in dry air has an oxide that is thinner. It does seem like also this oxide has voids, but not as many as the samples exposed in wet atmosphere.

The theoretical thicknesses of the oxides were also calculated based on the mass gain of the samples. The thickness of the oxides at A197 exposed in wet atmosphere at 800°C was calculated to 181 nm and 345 nm for the 20 hours and the 200 hours exposure respectively. The thickness of the oxide formed at A197 exposed in dry air for 200 hours was calculated to 115 nm.
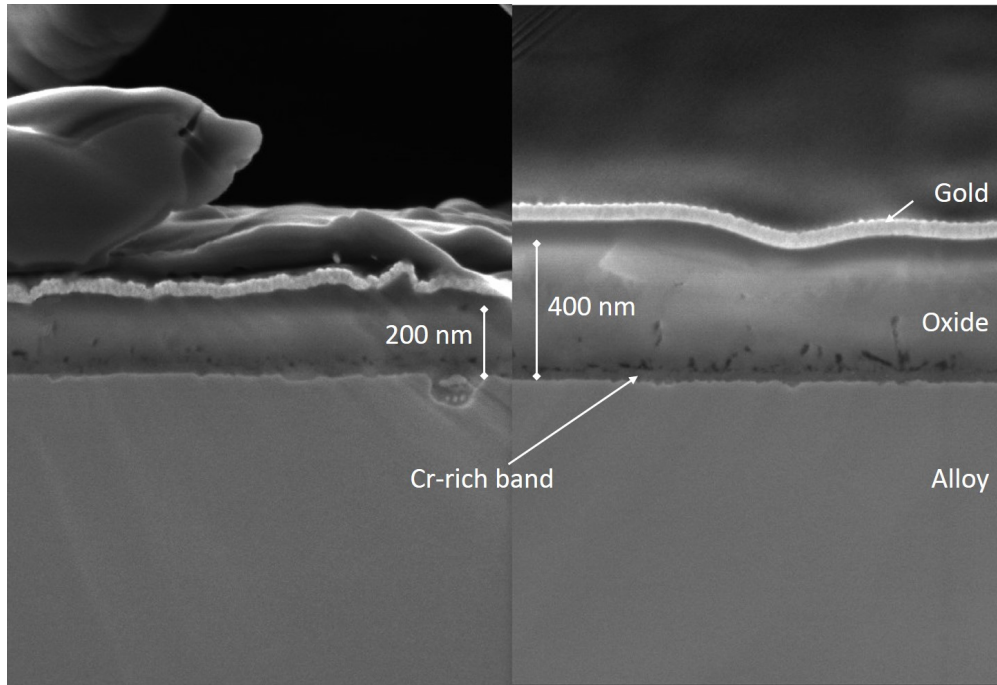
Figure 4.7: SEM images of the cross-section of A197 exposed in air containing 40% H_2O at 800°C for 20 hours (left hand side), and 200 hours (right hand side).
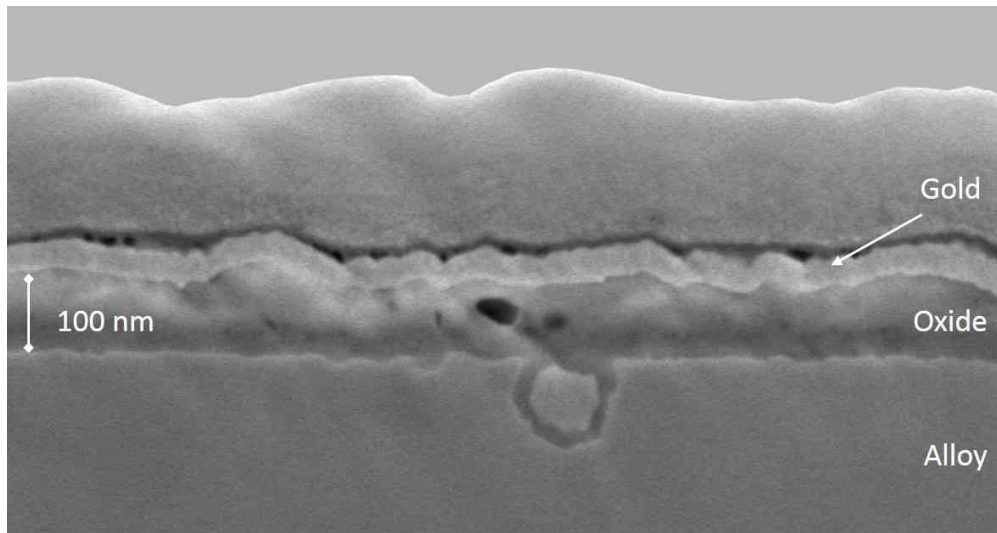
Figure 4.8: SEM image of the cross-section of A197 exposed for 20 hours in dry air at 800°C.

For further investigation of the oxide composition, STEM was used. Figure 4.9 and 4.10 show two examples of how the chemical composition of cations varies across the oxide of A197 exposed for 20 h in wet atmosphere at 800°C. The two plots show a Cr-rich band close to the oxide-alloy interface.
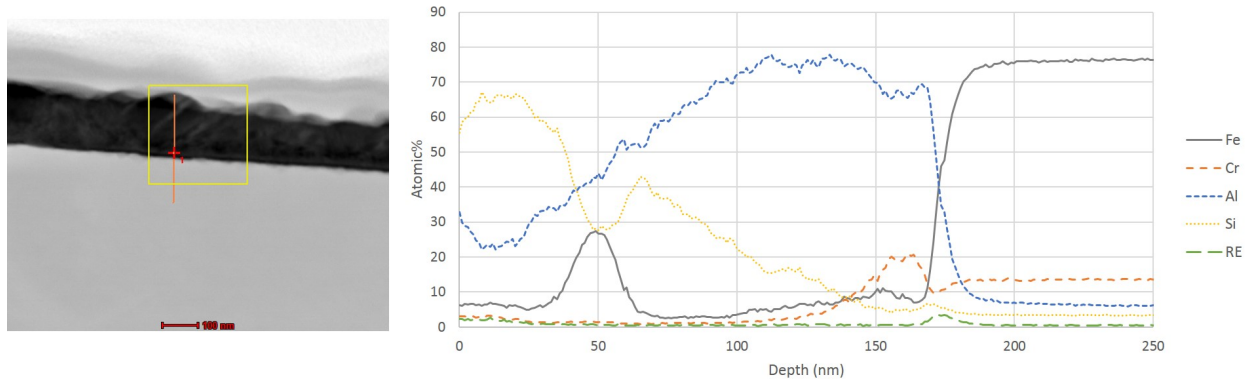
Figure 4.9: Oxide profile analysis 1 performed by TEM on A197 exposed in air containing 40% H_2O for 20 hours.
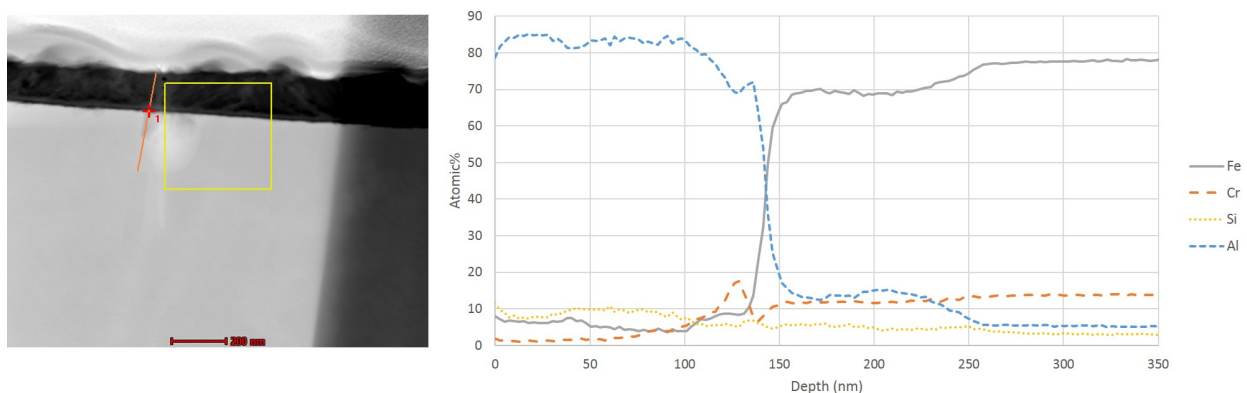
Figure 4.10: Oxide profile analysis 2 performed by TEM on A197 exposed in air containing 40% H_2O for 20 hours.

What also can be seen from the figures is that the Si content in the oxide is high and increases towards the surface of the oxide. However, the level differs between the two line scans. In the first scan, the silicon content decreases from above 60 atomic% to approximate 3 atomic% in the alloy. In the second line scan, the highest measured content is about 10 atomic%. In addition to the silicon, the first line scan also shows an iron-rich phase in the oxide. From the image it appears as a needle-like feature. The second line scan shows an aluminium enrichment in the upper part of the alloy. The both line scans have a peak in the Cr curve close to the oxide-alloy interface.

When an A14 sample exposed in wet atmosphere for 20 hours at 800°C was investigated by TEM it was not possible to find an increase of Si content in the oxide, see Figure 4.11.

31
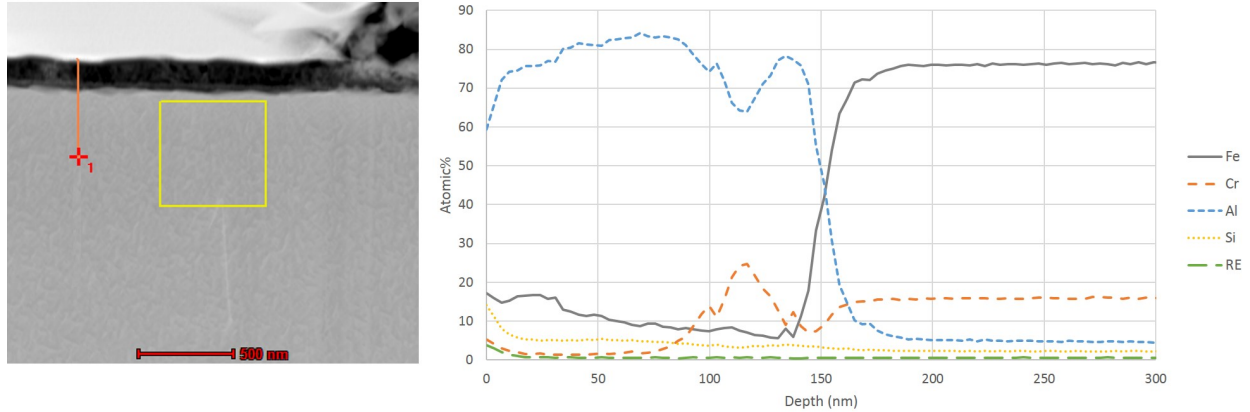
Figure 4.11: Oxide profile analysis performed by TEM of A14 exposed in air containing 40% H_2O for 20 hours at 800°C.

4.1.4 EDX Investigation of Si Content in the Vicinity of the Oxide Surface

The observed high Si content in the oxide of A197 exposed in wet atmosphere for 200 hours at 800°C was not expected, and was therefore further investigated. Figure 4.12a shows the EDX peaks of Al and Si from mentioned sample obtained from three different accelerating voltages. The yellow, red and green curves show the results from voltages of 20, 10 and 5 kV respectively. Since the interaction depth decreases when the accelerating voltage is decreased, the signals from the oxide scale should be more pronounced when a lower voltage is used. The intensity of the peaks are normalised based on the Al peak. As can be seen in the Figure 4.12a, the Si peak is higher, in relation to the Al peak, when the accelerating voltage lowered to 5 kV compared to when the higher voltages are used, indicating a higher Si content at the surface rather than subsurface.
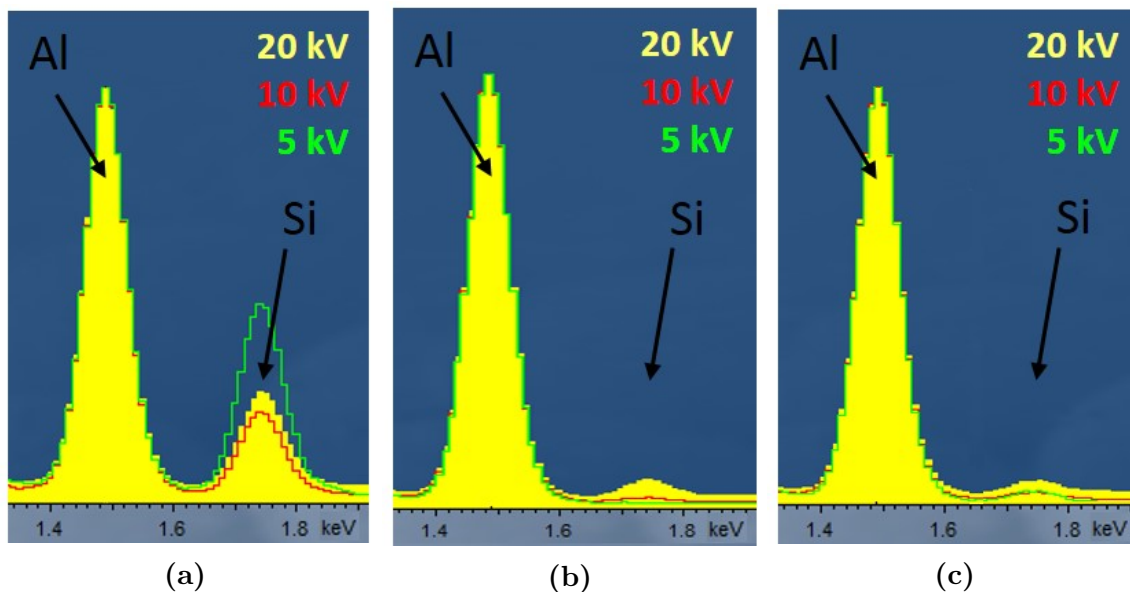
Figure 4.12: EDX analysis of a) A197, 200h, 40% H_2O, 800°C, b) A197, 200h, dry air, 800°C, c) A14, 200h, 40% H_2O, 800°C. Accelerating voltages: 20 kV (yellow), 10 kv (red) and 5 kV (green).

Figure 4.12b and 4.12c show the results from A197 exposed for 200 hours in dry air at 800°C and A14 exposed for 200 hours in wet atmosphere at 800°C. Here, the green 5 kV curves lie below the curves obtained from the higher voltages.

4.1.5 Crystal Structure Analysis of Oxides

XRD was used in order to find crystal phases in the oxides. Figure 4.13 shows the XRD patterns from A197 exposed for 200 hours in wet atmosphere, red curve, and in dry atmosphere, black curve, at 800°C. The figure also shows theoretical 2θ positions of possible α-Al_2O_3 and γ-Al_2O_3 peaks. Due to very thin oxide scales it can be hard to obtain a high amount of signals, and it is therefore hard to draw any conclusions from the XRD pattern. However there are some tendencies that the α-Al_2O_3 peaks fit the pattern obtained from the sample exposed in dry condition better than the other curve.

In the region 26 < 2θ < 40, there are several peaks found from the wet exposure that could not be found from the dry exposure. Those peaks fit the pattern of the aluminosilicat mullite. Other peaks have also been observed from both the dry and wet exposure, but they are still unidentified. However, from A197 exposed in wet atmosphere, it was possible to find peaks correlating to aluminium silicate hydroxide. This is another statement that confirms the hypothesis of hydroxylated grain boundaries.
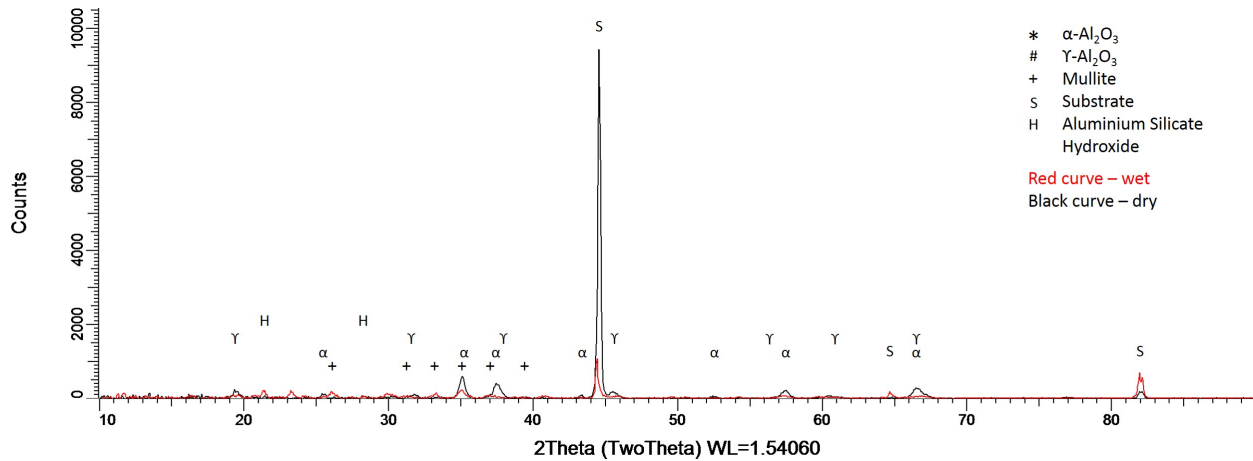
Figure 4.13: XRD pattern from A197 in air + 40% H_2O (red curve) and A197 in dry air (black curve), both exposed for 200 h at 800°C.

4.2 Exposures at 600°C

In following sections, the results from the 600°C exposures are presented. The result consists of evaporation data, mass gains, images obtained from SEM and EDX together with STEM investigation of the oxides.

4.2.1 $CrO_2(OH)_2$ Evaporation and Mass Change

The chromium evaporation from A14 and A197 was very low when exposed at 600°C. Figure 4.14 shows the evaporation rates measured at 600°C together with the rates measured at 800°C.
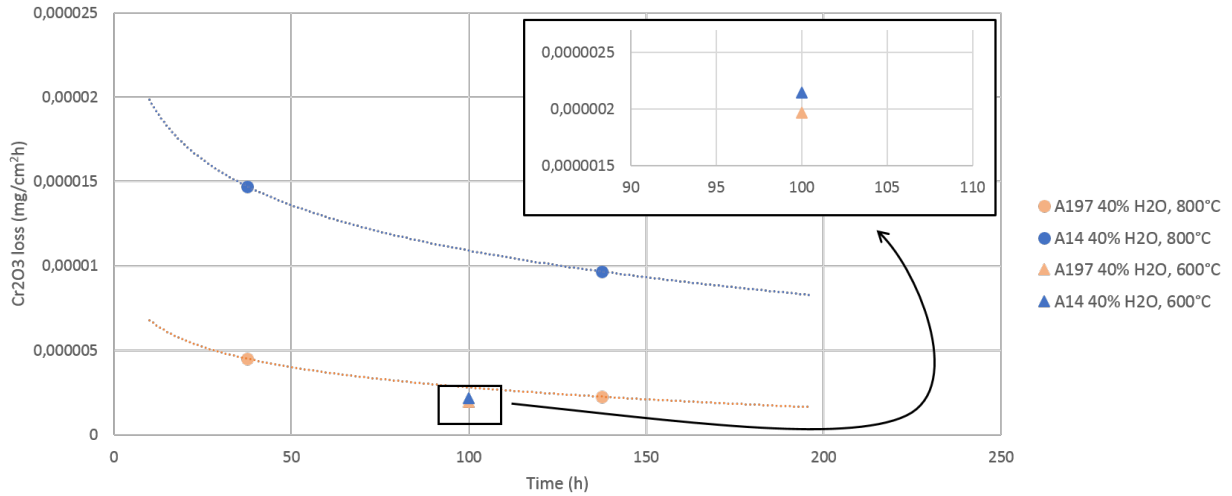
Figure 4.14: Chromia evaporation rate measured from A14 and A197 at 600°C and 800°C in air containing 40% water vapour, together with logarithmic trendlines.

Figure 4.15 shows the mass gains of the samples exposed at 600°C. The wet exposures of A197 shows higher mass gain than the dry exposures, but all measured mass gains are much lower than the mass gains measured from the 800°C exposures. The samples exposed for 200 hours do not show high increase in weight compared to the short exposures. It is also clear that the initial mass gains are much higher for A197 than for A14. However, after additional 180 hours, both increase in weight with nearly the same amount in the wet exposure.
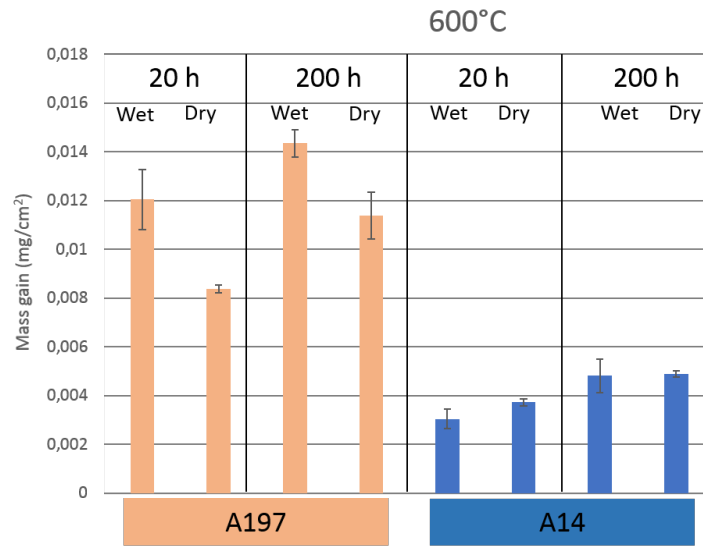
Figure 4.15: Mass gain due to oxidation of the alloys A14 and A197 in dry air and air containing 40% H_2O at 600°C.

4.2.2   Plan View Investigation of the Oxides

The SEM investigations of the oxides at A197 exposed at 600°C are shown in Figure 4.16. The base oxides are smooth, thin and fully covering. The RE particles are covered by thick Fe-oxide, see Figure 4.17. The size of the Fe-nodules is almost the same for all exposures. It may seem like the amount of RE particles is higher in Figure 4.18d, but this is probably not the case, since the RE particles are unevenly distributed in the alloy. Instead, it is possible to say that the number of particles stays constant during the exposures.
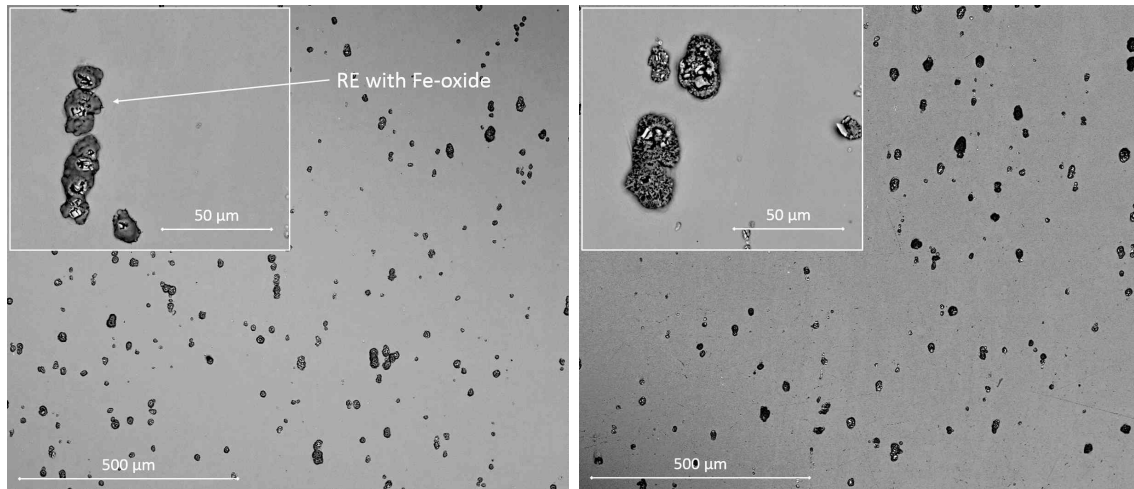
(a) A197, 20 h, 40% H$_2$O, 600°C.

(b) A197, 200 h, 40% H$_2$O, 600°C.
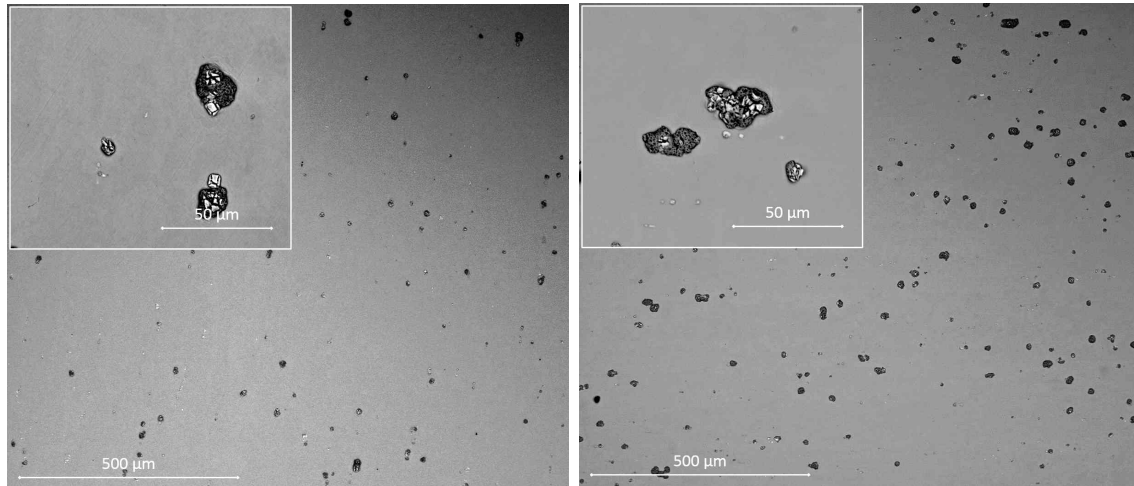
(c) A197, 20 h, dry air, 600°C.

(d) A197, 200 h, dry air, 600°C.

Figure 4.16: BSE images of A197 exposed at 600°C.
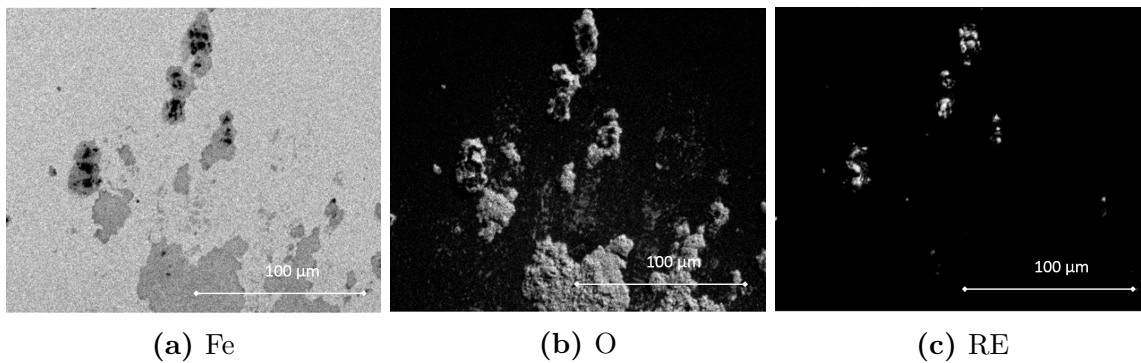
(a) Fe

(b) O

(c) RE

Figure 4.17: EDX mapping of A197 exposed in air with 40% H$_2$O at 600°C. Bright areas indicate locations with a higher concentration of respective element. The Fe detected in figure (a) is from the alloy that shines through thin oxide.

Also the oxide surfaces of A14 exposed at 600°C were investigated by SEM. Figure 4.18 shows the BSE images obtained. Since the grains in the alloy easily can be seen, the oxide seems to be very thin. The RE-particles are not covered by either thicker alumina oxide or Fe-oxide.

(a) A14, 20 h, 40% H_2O, 600°C.

(b) A14, 200 h, 40% H_2O, 600°C.

(c) A14, 20 h, dry air, 600°C.

(d) A14, 200 h, dry air, 600°C.
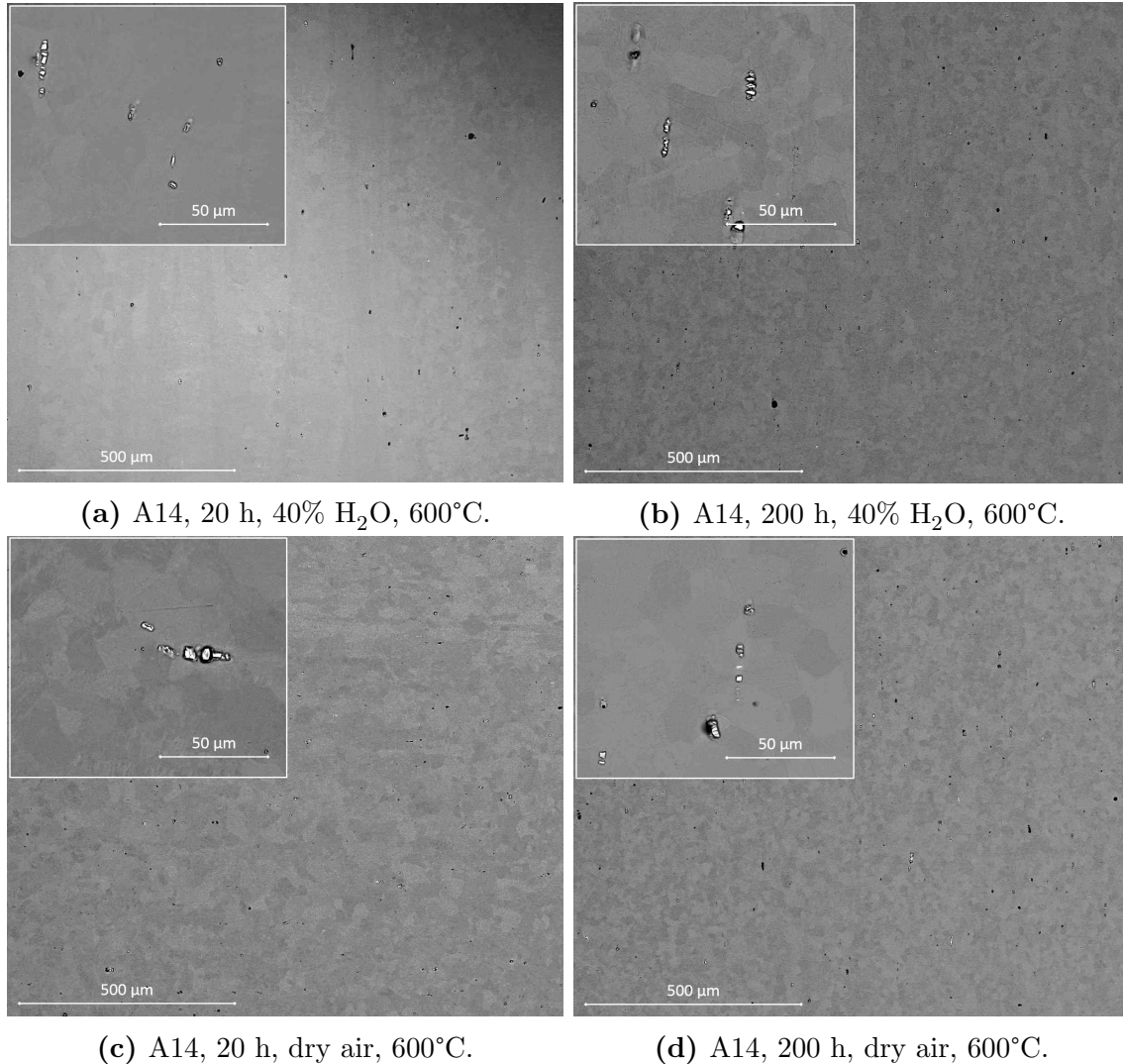
Figure 4.18: BSE images of A14 exposed at 600°C.

4.2.3 Cross-Section Investigation of the Oxides

A cross-section of A197 exposed in wet atmosphere for 200 hours at 600°C was prepared and investigated by Ultra 55 FEG SEM. Figure 4.19 shows a very thin, but dense oxide without any pores with a measured thickness of less than 50 nm. The theoretical thickness was calculated to 76 nm.
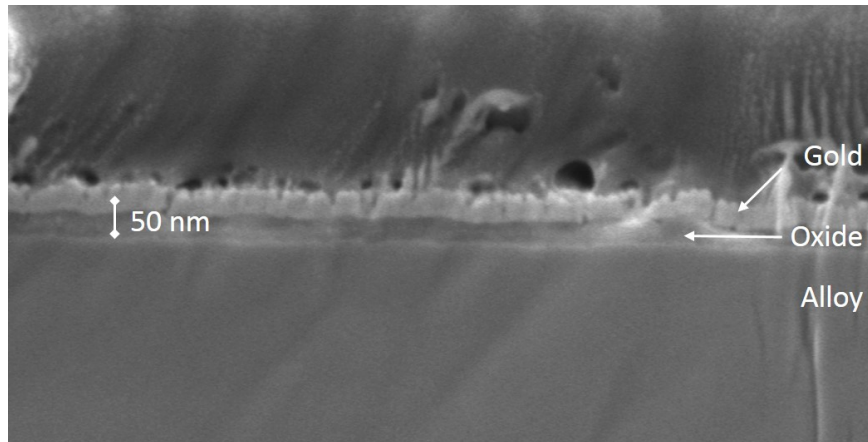
Figure 4.19: SEM image of the cross-section of A197 exposed for 200 hours in air containing 40% water vapour at 600°C.

4.2.4 A14 Field Experiment

A field experiment, where A14 was exposed in a test rig at PowerCell, was performed and investigated by TEM. The temperature and water content in air were similar to the ones used for the wet 600°C exposures performed in lab, but the gas flow velocity was considerably higher. Figure 4.20a shows a cross-section of Fe-oxide around a RE particle together with two line scans. The first line scan, Figure 4.20b, shows that there is a distinct peak in Al and Cr content at the interface between the outward growing Fe-oxide and the alloy. Figure 4.20c shows that an inward, mixed oxide is formed underneath the Fe-nodule.
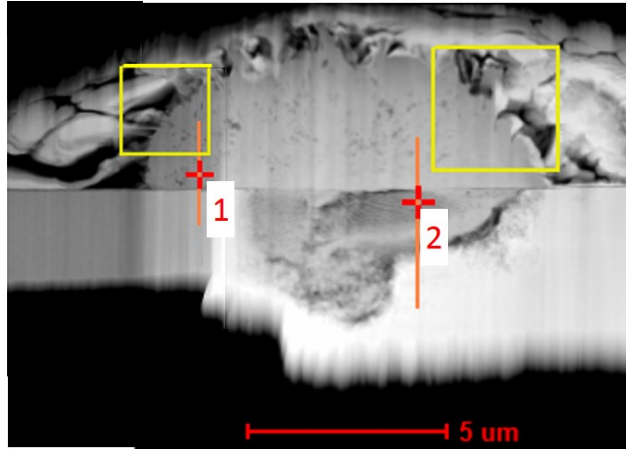
(a) Fe-nodule
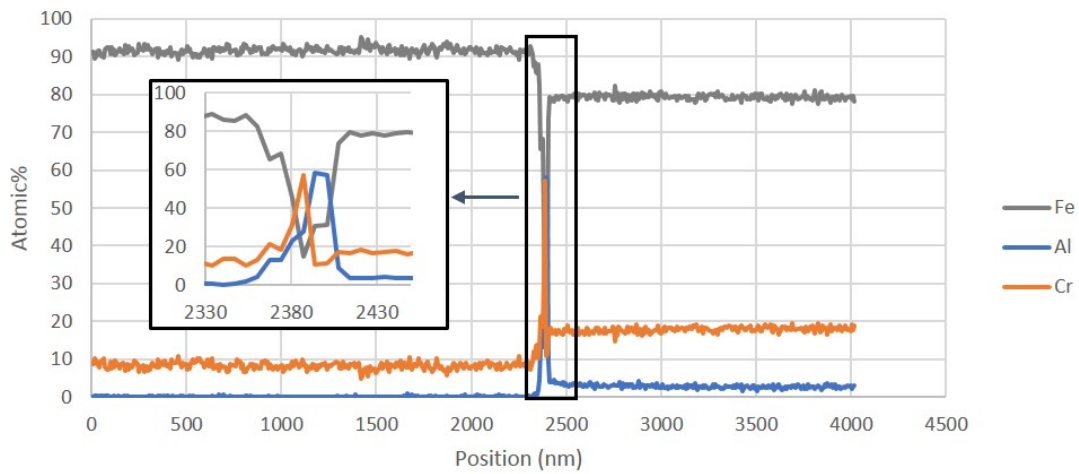
(b) Line scan 1
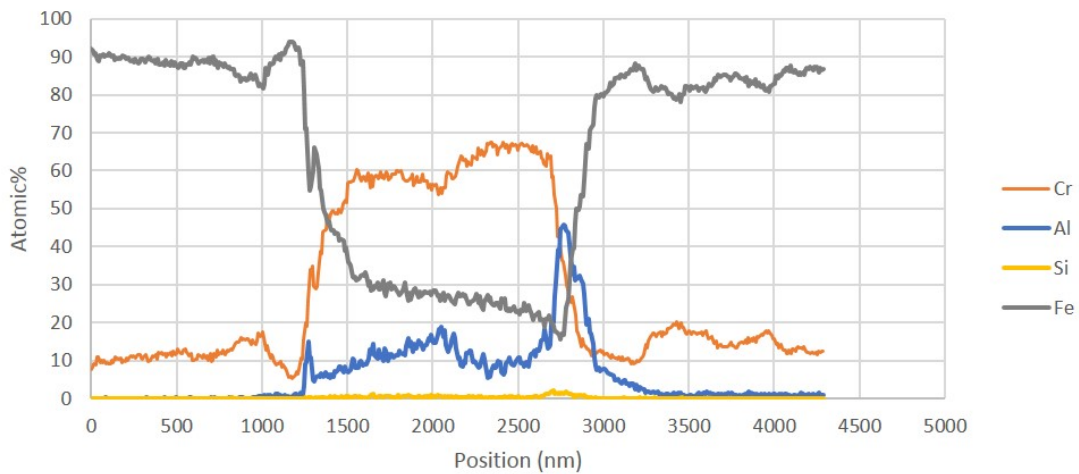
(c) Line scan 2

Figure 4.20: TEM image and line scans of A14 exposed for 90 hours in 40% H_2O at 600°C in a test rig at Powercell.

5

Discussion

This thesis is a part of a project testing new alloys for heat exchangers for e.g. fuel cells. Two of the most important criteria for the alloys to fulfil are that the chromium evaporation from the oxides should be low in order to not poison the catalysts used in the reformer in the fuel cell system, and that the oxide formed should be able to protect the material from corrosion. Since the chromium evaporation from both alloys at all different exposure environments were very low, it is possible to conclude that the alloys have passed the first criterion. Both A197 and A14 forms alumina in order to protect the materials from corrosion, meaning that the alloys are good candidates for the application.

As the results have shown, all exposures performed at 800°C gave rise to protective oxides where no harmful corrosion was observed. However, when the temperature was decreased to 600°C, the morphology of oxides was changed, especially for the A197 alloy where flake-like Fe-oxide was observed around the RE particles.

In following sections the effect of temperature, water vapour and alloy composition will be discussed.

5.1   Mass Gain and Oxide Thickness

A general trend for the alumina-forming alloy A197 exposed at both 800°C and 600°C, is that the mass gain, in contrast to Cr-losing stainless steels, is higher if the alloy has been exposed in wet atmosphere compared to dry air. From that it can be concluded that water vapour has an impact on the oxidation. Furthermore, the mass gain, both from the dry and the wet exposures, is high in the beginning and then decreases or nearly stagnates in the progression. Thus, it is possible to say that the initial part of the oxidation is very important. This was also stated by Liu et al (2005), meaning that the result in this thesis is reliable. Mortazavi et al. (2018) showed that when water is present and interacts with RE particles in the oxide, the grain coarsening is delayed since the grain boundaries are hydroxylated. Thus, the transport paths for water or water equivalents towards the metal/oxide interface remain open for a longer time and the mass gain increases rapidly as a consequence. In other words,

the high mass gain observed from A197 in the initial part of the oxidation is due to a high grain boundary density, in combination with presence of RE ions. Since diffusion within the Al_2O_3 crystals is not kinetically favourable, the oxidation rate decreases rapidly after the set in of potential grain coarsening. If experiments with exposure times shorter than 20 hours would have been performed it is possible that a mass gain curve showing a sub-parabolic shape could be observed. In order to confirm this theory, rate of grain coarsening needs to be studied, this was however not studied in this thesis.

The other alumina-forming alloy A14 also showed the highest mass gain rate in the initial part of the oxidation. However, the difference in mass gain between the wet and dry exposures was not as pronounced as for A197. The mass gain of all A14 exposures, except for short dry exposure at 800°C, are lower than corresponding exposures of A197. This can be explained by the much lower number of RE particles in A14 compared to A197.

In previous studies it has been shown that water vapour stabilises the transient γ-Al_2O_3 phase. From the XRD work performed in this thesis, it was somewhat hard to prove this hypothesis since the oxides were very thin and therefore difficult to investigate. In order to investigate the presence or absence of α-Al_2O_3, another analysis method, such as Convergent Beam Electron Diffraction (CBED) would be to preferrable. It is possible that also hydroxylated species could be detected by this method.

The temperature has a major impact on the chemistry, oxidation rate and the morphology of the oxides. Both A197 and A14 show much higher mass gain at 800°C compared to the exposures at 600°C since it is more challenging to reach the activation energy when the temperature is lower. From the SEM cross-section analysis it was shown that the oxide base layer formed at A197 exposed in wet atmosphere for 200 hours at 600°C was about a tenth of the thickness of the oxide formed from same exposure but performed at 800°C. Also the formation of oxide around the RE particles differs a lot when comparing the mentioned exposures. For the 600°C exposures of A197, the particles were covered by Fe-oxide, since the slow kinetic prevents the formation of Al_2O_3, which was observed around the RE particles at the higher exposure temperature.

Also the mass gain-based calculations of oxide thickness showed that the oxide scales should be thinner, around 70-80 nm, for the 600°C exposures, but not as thin as measured by SEM, where the thickness was shown to be around 30 nm. It proves that the aluminum oxide thickness estimate from the mass gain has been overestimated due to the locally rapid growing Fe-oxide covering RE particles within the first 20 hours.

Laboratory exposures of A14 at 600°C did not, in contrast to A197, show formation of Fe-oxide around the RE particles. This is probably due to the higher content of both Al and Cr in A14, making it easier for alumina to form even if the temperature is low. Therefore, it may seem like A14 is to prefer when choosing a material for high temperature application, but it is important to stress that low concentrations of Al and Cr are wanted in order not to challenge the mechanical properties of the alloy. If longer exposures of A14 were to be run, it is possible that those mechanical related defect could be observed.

The STEM analysis of the A14, Figure 4.20a, exposed in the test rig at PowerCell showed formations of Fe-oxide. The reason to why Fe-oxide was found at this sample and not at the ones exposed in lab are not fully explained. A hypothesis is that the sample in the test rig had a longer heating-up time, since the reformer was not pre-heated as the furnaces used in lab. Residence time at even lower temperatures than 600°C are even more challenging for the selective oxidation of aluminium. This, together with an unstable temperature during the exposure, probably lead to formations of Fe-oxide.

Furthermore, the analysis showed that Fe-nodules and the alloy are separated by Al- and Cr-rich regions. Line scan 1 shows distinct peaks in the curves of both Cr and Al, which resembles the ordinary base oxide layer where the formation of Cr_2O_3 makes it possible to form the protective alumina.

Line scan 2 does not show those distinct peaks, but a much larger area beneath the Fe-nodule where the composition of the oxide is changing. If the position 600 to 1400 nm in Figure 4.20c is studied more closely, it can be seen that the Cr content increases just before a small Al-peak. Again, this behaviour resembles of the base oxide. However, it seems like the aluminium concentration in this region was not high enough in order to form the alumina scale needed for corrosion protection. After the mentioned region, both Cr and Al concentration increases. At position 2800 nm the concentration of Al is high enough in order to form the protective alumina layer. This is the new interface between the oxide and the alloy. Except for the detection of Fe, Al and Cr, also Si was found in line scan 2. Even if the concentration of Si is low, a small peak can be found just close to the Al peak. It indicates that Si, just like Cr, has a third element effect and thus supports the formation of the protective scale.

Even if this was observed for A14 it is likely, due to what have been seen by SEM and discussed above, that this self-healing effect is present also in A197. Since the Si concentration is higher in A197 than in A14, it is likely that the Al_2O_3 scale formation underneath an Fe-nodule sets in even earlier. If so, it is possible that A197 would be a very good candidate when selecting materials for corrosive high temperature environment, even if Fe-oxides are present in early stage of the oxidation.

5.2   Oxide Composition

Liu et al. (2007) and Engkvist et al. (2009) showed that the oxide composition formed from a FeCrAl alloy differs depending on exposure temperature. The studies, performed at 500°C, 700°C and 900°C showed that the the Cr-band, which is a remnant from the initial oxidation, was found only in the exposures performed at the two higher temperatures. Since the temperatures used in this thesis, 600°C and 800°C, lies between the temperatures from the previous studies, the results can be put in context. The depth profile analysis performed by TEM showed that the Cr-band was present at 800°C, which is in line with the previous

results. The studies also showed that the Mg and Fe content was increasing toward the oxide-gas interface. In this thesis, the same trend was found for Fe. Mg was not detected at all by TEM. Furthermore, Liu showed that the alumina was of two types, α-Al_2O_3 above the Cr-band, and γ-Al_2O_3 between the Cr-band and the alloy. This was not observed in this thesis since no crystal phases analysis was performed by TEM.

TEM investigation of samples exposed at 600°C was not performed before handing in of this thesis. Therefore, it is not possible to tell if those oxides have the characteristic Cr-band or if the composition is of the mixed type as shown from the 500°C exposures performed by Engkvist.

A novel finding in this study is that an FeCrAl alloy may form an oxide with a high content of Si. This was the case when A197, containing 1-2% Si, was exposed at 800°C in wet atmosphere. This was observed by XRD, TEM and SEM from both the long and short exposure, but not from the other exposures of either A197 in dry air or A14 in wet or dry air.

Since this has not been observed before, it was of highest interest to investigate it more closely. An initial hypothesis was that the Si detected did not originate from the alloy itself, but from the external environment. It was likely to think that the oxidising, water rich environment in the furnace liberated Si from the reaction tube [31], and that this substance was subsequently incorporated in the growing oxide scale. However, since the increase of Si was not observed in the oxide formed in the wet exposures of A14, this theory was rejected.

When comparing the oxide at A197 with the results of Liu et al. (2007) it seems like the Si in A197 oxide showed almost the same behaviour as Mg did since the concentration of both elements increased towards the oxide/gas interface forming a secondary type oxide. In the study performed by Liu, this oxide was found to be $MgAl_2O4$, while the XRD work performed in this thesis indicated formation of mullites. This was very interesting since the chemistry of the two elements are very different regarding properties such as electronegativity and valency.

6

Conclusions

From this thesis, some conclusions can be made regarding the oxidation behaviour of FeCrAl alloys:

- It has been shown that the Cr-evaporation from both A14 and A197 exposed in both dry and wet atmosphere at 600°C and 800°C was very low. This is very important since the evaporated compound poisons the catalyst used in the ATR.

- Both A14 and A197 were able to form an alumina scale at the surface of the alloys, meaning that the materials are protected from corrosion. However, A197 showed development of Fe-oxide around RE particles when exposed at 600°C, but since the growth of it ceased, it is possible that the corrosion resistance of the alloy is not affected.

- The mass gain of the alloys was, in general, higher if water vapour was present during the exposure due to an interplay with RE particles in the oxide. Results indicating that water stabilises transient Al_2O_3 have also been presented in this thesis.

- The oxide formed at A197 contained a surprisingly high amount of Si when exposed in wet atmosphere. It is suggested that Si has a third element effect, meaning that the element promotes the formation of protective alumia.

7

Outlook

Since it has been shown that the oxidation rate is highest in the initial part of the oxidation it would be interesting to investigate the first hours more closely. Especially in the case of the 600°C exposures of A197 since the Fe-oxides were developed during this period. To do so, it is possible to use the same experimental method used in this work but decreasing the exposure time. It is also possible to use a thermobalance where both the temperature and the weight of the sample can measured continuously during the exposure.

On the other hand, since the mass gain and the size of Fe-rich oxides covering the RE particles in A197 seems to cease with time, which is important for thin components. Instead, longer exposures need to be performed in order to investigate the long time effect of the base oxide in general and the Fe-oxides in particular.

In order to improve the understanding of oxidation of FeCrAl alloys it is important to identify the crystalline phases of alumina in the scale. Since this was not possible in this thesis, it is suggested to be a future work. Another observation that remains uninvestigated is the void-like structures found in the SEM images of the oxide cross-sections.

As mentioned earlier, the high content of Si needs to be investigated more closely. That could be done by TEM or Auger Electron Spectroscopy. In this thesis only the cross-sections of A197 and A14 exposed in wet atmosphere at 800°C have been studied by TEM. It is therefore of highest interest to also study the oxides formed at the lower temperature.

The BSE and EDX images of A197 exposed for 200 hours at 800°C indicated that the alloy surrounding the contained a lower amount of Al. It was suggested that the growth of thicker alumina depletes the alloy of Al. However, since it was not possible to prove this phenomena in this thesis, it is recommended as a future work.

It was said in this thesis that the interplay of RE elements and water held the grain boundaries open in the initial part of the oxidation to prevent grain coarsening. However, since the grain size of the oxide was not investigated, it is not possible to state this hypothesis. Therefore, the the grain size needs to be measured both before and after the oxidation in order to find if grain coarsening has set in or not.

[1] H. Asteman, K. Segerdahl, J.E. Svensson, L.G Johansson, M. Halvarsson, and J. Eu Tang. "Oxidation of Stainless Steel in H 2 O/O 2 Environments – Role of Chromium Evaporation". In: *Materials Science Forum* 461 (Jan. 2004).

[2] H Götlind. *High Temperature Corrosion of the FeCrAl Alloy Kanthal AF*. Göteborg : Chalmers University of Technology, 2007.

[3] P. Prescott and M.J. Graham. "The Oxidation of Iron-Aluminum Alloys". In: *Oxidation of Metals* 38 (1992), pp. 73–87.

[4] IPIECA. *Heat Exchangers*. Feb. 2014. URL: http://www.ipieca.org/resources/energy-efficiency-solutions/efficient-use-of-heat/heat-exchangers/ (visited on 02/05/2019).

[5] *Heat exchanger (Energy conversion)*. Encyclopædia Britannica, inc. Apr. 2018. URL: https://www.britannica.com/technology/heat-exchanger (visited on 02/05/2019).

[6] S.T. Tu and G.Y. Zhou. "Compact Heat Exchangers in Clean Energy Systems". In: *Handbook of Clean Energy Systems* (2015).

[7] West Coast Regasketing WCR. *This is a Plate Heat Exchanger*. 2019. URL: https://www.wcr.se/plateheatexchangers.html (visited on 05/07/2019).

[8] K. Liu, C. Song, and V Subramani. *Hydrogen and syngas production and purification technologies*. American Institute of Chemical Engineers, 2010.

[9] H. Falk Windisch. *Improved Oxidation Resistance and Reduced Cr Vaporization from Thin-Film Coated Solid Oxide Fuel Cell Interconnects*. Göteborg : Chalmers University of Technology, 2017.

[10] "DerSilberspiegel [CC BY-SA 4.0 (https://creativecommons.org/licenses/by-sa/4.0)] via Wikimedia Commons". URL: https://upload.wikimedia.org/wikipedia/commons/6/6a/Ellingham_Richardson-diagram_english.svg.

[11] D.J. Young. *High temperature oxidation and corrosion of metals*. second. Amsterdam ; Oxford ; Cambridge : Elsevier, 2016.

[12] *Ellingham Diagrams*. 2008. URL: https://www.doitpoms.ac.uk/tlplib/ellingham_diagrams/index.php (visited on 01/29/2019).

[13] G. Meier N. Birks and F. Pettit. *Introduction to the High Temperature Oxidation of Metals*. Cambridge: Cambridge University Press, 2009.

[14] B. N. Popov. *Corrosion Engineering*. Amsterdam, Netherlands : Elsevier, 2015.

[15] V. Babic, C. Geers, B. Jönsson, and I Panas. "Fates of Hydrogen During Alumina Growth Below Yttria Nodules in FeCrAl(RE) at Low Partial Pressures of Water". In: *Electrocatalysis* 8.6 (2017), pp. 565–576.

[16] Johan Eklund. *Material solutions for mitigating high temperature corrosion in biomass- and waste-fired boilers : utilizing novel FeCrAl alloys and HVAF-sprayed Ni-based coatings*. Göteborg : Chalmers University of Technology, 2018.

[17] J. Froitzheim, H. Ravash, E. Larsson, L.G. Johansson, and Svensson J.E. "Investigation of Chromium Volatilization from FeCrInterconnects by a Denuder Technique". In: *Journal of The Electrochemical Society* 157.9 (2010), B1295.

[18] *Safety and Health Topics - Hexavalent Chromium - Occupational Safety and Health Administration.* URL: https://www.osha.gov/SLTC/hexavalentchromium/ (visited on 03/15/2019).

[19] Kevin G. Field, Mary A. Snead, Yukinori Yamamoto, and Kurt A. Terrani. *Handbook on the Material Properties of FeCrAl Alloys for Nuclear Power Production Applications (FY18 Version: Revision 1).* Aug. 2018. DOI: 10.2172/1474581.

[20] F. Liu. *Microstructural investigation of high temperature oxidation of Al2O3-forming and Cr2O3-forming steels - The influence of water vapour.* Göteborg : Chalmers University of Technology, 2008.

[21] H. Götlind, F. Liu, J-E. Svensson, M. Halvarsson, and L-G. Johansson. "The Effect of Water Vapor on the Initial Stages of Oxidation of the FeCrAl Alloy Kanthal AF at 900 ℃". In: *Oxidation of Metals* 67 (2007), pp. 251–266.

[22] F. Liu, H. Gölind, J-E. Svensson, L-G. Johansson, and M. Halvarsson. "Early stages of the oxidation of a FeCrAlRE alloy (Kanthal AF) at 900 ℃: A detailed microstructural investigation". In: *Corrosion Science* 50.8 (2008), pp. 2272–2281.

[23] J. Engkvist, S. Canovic, F. Liu, H. Götlind, J.E. Svensson, L.G. Johansson, M. Olsson, and M. Halvarsson. "Oxidation of FeCrAl foils at 500–900℃ in dry O2 and O2 with 40% H2O". In: *Materials at High Temperature* 26 (2009).

[24] N. Mortazavi, C. Geers, M. Esmaily, V. Babic, M. Sattari, K. Lindgren, P. Malmberg, B. Jönsson, M. Halvarsson, and J. E. et al. Svensson. "Interplay of water and reactive elements in oxidation of alumina-forming alloys". In: *Nature Materials* 17.7 (2018), pp. 610–617. DOI: 10.1038/s41563-018-0105-6.

[25] J. Eklund, B. Jönsson, A. Persdotter, J. Liske, J.-E. Svensson, and T. Jonsson. *The influence of silicon on the corrosion properties of FeCrAl model alloys in oxidizing environments at 600 ℃.* Vol. 144. 2018, pp. 266–276. DOI: 10.1016/j.corsci.2018.09.004.

[26] J Checmanowski, Matraszek A, I Szczygieł, and Szczygieł B. "High-temperature oxidation of FeCrAl alloy with alumina–silica–ceria coatings deposited by sol–gel method". In: *Journal of Thermal Analysis and Calorimetry* 113 (2013), pp. 311–318.

[27] R.F. Egerton. *Physical Principles of Electron Microscopy.* Springer International Publishing, 2016.

[28] J. I. Goldstein, D. E. Newbury, J. R. Michael, N. W. M. Ritchie, J. H. J. Scott, and D. C. Joy. *Scanning Electron Microscopy and X-Ray Microanalysis.* Springer, 2018.

[29] C. Göbel. *Corrosion of Ferritic Stainless Steels Used in Solid Oxide Fuel Cells.* Göteborg : Chalmers University of Technology, 2018.

[30] *High Temperature Properties.* Specialty Steel Industry of North America: SSINA. 2019. URL: http://www.ssina.com/composition/temperature.html.

[31] Elizabeth J. Opila, James L. Smialek, Raymond C. Robinson, Dennis S. Fox, and Nathan S. Jacobson. *SiC Recession Caused by SiO2 Scale Volatility under Combustion Conditions: II, Thermodynamics and Gaseous-Diffusion Model.* 1999.

Appendix 1

Experimental Protocol

Start up

1. The temperature, steam content (40% H_2O) and flow rate (3000 ml/min for wet exposures, 6000 ml/min for dry exposure) in the furnace was measured by thermocouple, dew point thermometer and flowmeter respectively.

2. Three cleaned, grinded samples were weighted on a microbalance and placed in a sample holder in the horizontal tubular reactor.

3. The tube was inserted in the furnace while the gas flow was off.

4. The end cap, denuder and wash bottle were connected to the tube. The denuder and part of the tube outside the furnace was isolated by heating cord and aluminium foil.

5. The gas flow, either dry or humidified with water vapour, was started. The exposure time was counted from the turn on of gas.

Shut down

1. The counting exposure time and the gas flow were turned off.

2. The aluminium foil and the heating cord were removed.

3. The wash bottle was detached. The denuder was removed and placed in a cleaned measuring flask.

4. The end cap was removed and the inner tube was taken out of the furnace. The samples were placed in an desiccator placed in the microbalance room.

5. The denuder tube were rinsed with 25 ml mq-water.

6. The solution in the wash bottle were condensed to approximate 20 ml.

7. The weight of the samples was measured.

8. The chromium concentration of the solutions from the denuder and wash bottle was measured by UV/Vis spectrometer (wavelength: 370 nm, Abs. range 0.2-1.6)

Denuder Change For the long exposures performed at 800°C, the denuder was changed in the middel of the exposure. The change was performed as follows:

1. The gas flow was turned of.

2. The aluminium foil and heating cord were removed

3. The wash bottle and denuder were detached and replaced by a new denuder and wash bottle.

4. The system was isolated by aluminium foil and heating cord.

5. The gas flow was turned on.

6. The chromium concentration in the denuder and wash bottle was measured as described in the "Shut down" list above.